Chapter 1
INTRODUCTION AND LITERATURE REVIEW

1.1 Introduction

Condensed matter systems serve as an exciting field of research for studying the physics of classical and quantum many-body phenomena [1]. In most of the systems, the interactions between its microscopic constituents cooperate, or only compete weakly, to drive the pertinent degrees of freedom into some ordered state. Examples include simple inorganic solids, metals, liquid crystals, conventional superconductors, and many magnetically ordered systems such as ferromagnets and antiferromagnets [2]. Alternatively, there is a frustrated class of materials that exhibits strongly competing interactions instead of cooperating interaction, with no clear choice of the ultimate ground state of the system [3]. There can be many degenerate or near-degenerate states at low energies, opening a route toward unconventional phases leading to exotic low-energy excitations [4]. Most of the archetypical examples of highly frustrated condensed matter systems have emerged in the domain of magnetism [5], [6].

Quantum magnetic materials, for example, could be at the forefront of an upcoming revolution in electronics. Future electronic devices like long-lasting nanoscale memories or noise-resistant quantum computing platforms can be realized by exploiting the dynamics of magnetic molecular systems. Such systems owe their magnetic properties to the magnetic moment or spin of their atoms and the subsequent arrangements of these spins [7]. Since the spin is a genuinely quantum mechanical phenomenon, these systems are also often used as

real testbeds for the study of quantum behavior [8]. The understanding of physical processes at the atomistic and molecular level requires detailed knowledge of the system's dynamics at the quantum mechanical level [9].

These are interesting systems where quantum fluctuation of spins eludes the possibility of conventional long-range ordering, down to the lowest possible temperature [10]. Such systems are characterized by broken symmetries even at zero temperature. There are few magnetically frustrated rare earth oxides, where the emergence of quantum critical point and followed up quantum phase transition are probable [11], [12]. Categorically "quantum spin-ice," an exotic magnetically frustrated system, had attracted researchers to establish a clear understanding of its low-temperature phases, where ice like spin correlation, along with significant quantum fluctuation, exists at finite temperatures [13], [14]. The transition (ordering) is expected to occur at a much lower temperature with respect to their Curie-Weiss temperature due to extremely frustrated antiferromagnetic (AFM) exchange interaction between the spins of nearest neighbor magnetic ions. These behavior become more prominent when one deals with them in a regime where semi-classical phenomena are dominant.

Pyrochlore oxides come under the class of magnetically frustrated systems and have found application in magneto-caloric, dielectrics, fast-ion conductors, electrocatalysts, nuclear waste encapsulation, sensors, solid oxide fuel cell and transistors [15]–[17]. The spin arrangement in such systems is almost ideal Ising like following the water ice model along [111] direction in the tetrahedra of pyrochlore lattice [18]. In antiferromagnetic pyrochlores, the possible frustrated random arrangement of spins belonging to a single tetrahedron lifts the degeneracy, and the system could be driven to an ordered state through a disordering mechanism, establishing a collinear spin arrangement. Even in this condition, the system

remains frustrated, and there is no global order by the disorder. Conventional spin-glass transition in these types of classical pyrochlore antiferromagnet leads to a freezing behavior and trapping of spins into a metastable state in an otherwise disorder free system. Hence it was inferred that perturbation occurred due to coupling between spin and lattice degrees of freedoms, and this prompted the researchers to investigate the phenomenon of spin-lattice coupling in such spin disordered systems in a more detailed manner [19], [20]. Such perturbations in spin-lattice coupling could be realized through the application of chemical pressure in the lattice [21]. This coupling leads to the global lifting of magnetic degeneracy and drives the system to long-range magnetic order followed by cubic to tetragonal lattice transition. The magnetic ground state also depends upon the spin configuration on the lattice site, which could be either Ising, XY, or of Heisenberg type. For e.g., the behavior of the nearest neighbor Ising pyrochlore antiferromagnet differs markedly from that of the nearest-neighbor classical Heisenberg antiferromagnet where a coplanar order by disorder develops on a 2D Kagome lattice [22]–[24]. While no transition is seen in the pyrochlore Heisenberg system, the pyrochlore lattice with XY type of spins where spins lie in easy planes perpendicular to the local <111> direction displays a phase transition to long-range order. Monte Carlo simulations found that the Ising antiferromagnet or ferromagnet with spins along local <111> direction is a relevant model to explain spin ice materials, which does not order down to the lowest temperature [4], [24]. Pinnetes *et al.* (2002) studied a classical Heisenberg pyrochlore antiferromagnet in which the exchange interaction varies between a pyrochlore lattice and a face-centred cubic lattice. The exchange interaction plays a major role that could propel a system to order into a collinear state whose energy is greater than the classical incommensurate ground state predicted by the mean-field theory [25].

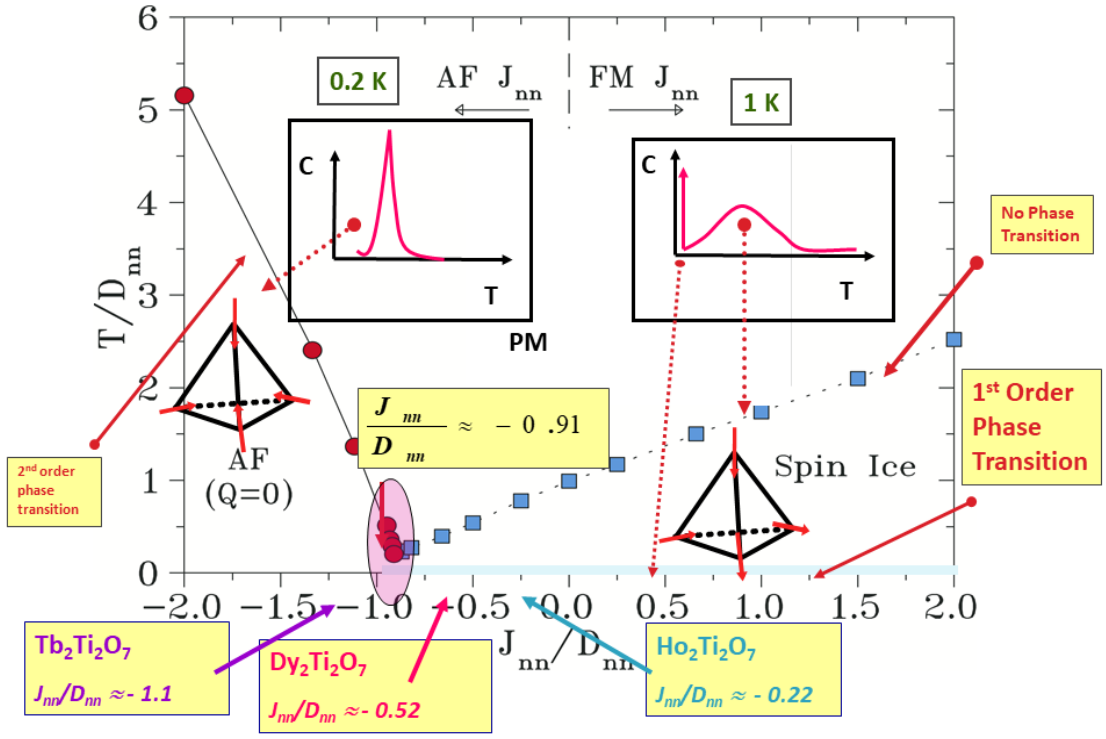

Figure 1.1 Dipolar Spin Ice Model (DSIM) which presents the possibility for inducing long-range ordering by varying the complex dipolar and exchange interaction in spin disordered systems. [26]

Later, den Hertog and Gingras explained the phase diagram based upon the dipolar spin-ice model (DSIM) as shown in **Figure 1.1,** which suggests that the Ising pyrochlore magnet reveals the spin ice configuration which persists till "$J_{nn}/D_{nn} \sim -0.91$", where J_{nn} and D_{nn} are the nearest neighbor exchange and dipolar interaction respectively. This threshold decides the stability regime for the spin ice systems. For "$J_{nn}/D_{nn} < -0.91$", the system undergoes a second-order phase transition to the nearest-neighbor antiferromagnetic ordering, where spins point "all in or all out" for a given tetrahedron [24]. To date, no pyrochlore system having Ho^{3+} as a magnetic ion had been reported to transit beyond -0.91 (J_{nn}/D_{nn}) in the phase diagram as proposed on the basis of DSIM [26]. Spin ice materials are the clearest examples of such

highly frustrated systems. They offer an unparalleled opportunity for the study of frustration in magnetic systems at both an experimental and a theoretical level.

Chemical pressure serves as an excellent aid to tune the J_{nn}/D_{nn} ratio, which in turn can shift the system in a different regime of magnetically ordered phase, as shown in **Figure 1.1.** The chemical pressure can be generated through the inclusion of elements having varying ionic radii, e.g., positive chemical pressure can be generated by the inclusion of Ge^{4+} in the $Ho_2Ti_2O_7$ matrix, whereas negative chemical pressure can be generated using Ti^{4+} at the Ge site in $Ho_2Ge_2O_7$.

The present thesis deals with the comprehensive study of the synthesis, crystal structures and magnetic properties of a class of magnetically frustrated pyrochlore oxide systems $Ho_2Ge_xTi_{2-x}O_7$ with varying x. The one end of this system is cubic (space group – $Fd\bar{3}m$) while the other end is tetragonal (space group - $P4_12_12$), having an entirely different kind of spin arrangement [27], [28]. The key related concepts are discussed as follows.

1.2 Magnetic interactions

Magnetism continues to be a rich source of scientific inquiry, with associated technological implications. Fine control over the strength and directionality of magnetic interactions between magnetic elements leads to a plethora of tenable ground states of spin-ice, spin glass, spin liquid, and unconventional long-range ordering through an order by disorder mechanism in the pyrochlore lattices. In this section, we highlight the persistent magnetic interactions toward understanding and controlling such ground states. The major magnetic interactions are described as follows.

1.2.1 Dipolar Interaction

Dipole-dipole interaction between two magnetic moments is proportional to $[(\mu_1\mu_2)/r_{nn}^3]$ $(3\cos^2\theta - 1)$. The field strength of a dipole falls off as $1/r_{nn}^3$ but the rate of a process driven by dipolar interactions falls off as $1/r_{nn}^6$. The term involving the $y = 3\cos^2\theta - 1$ is particularly important, as shown at the bottom of **Figure 1.2**. It is seen that the values of y are symmetrical about $\theta = 90°$. It is interesting to note that $y = 0$ for $\theta = 54°$ and 144°, i.e., for these particular angles, the dipolar interaction disappears even when the spins are close in space.

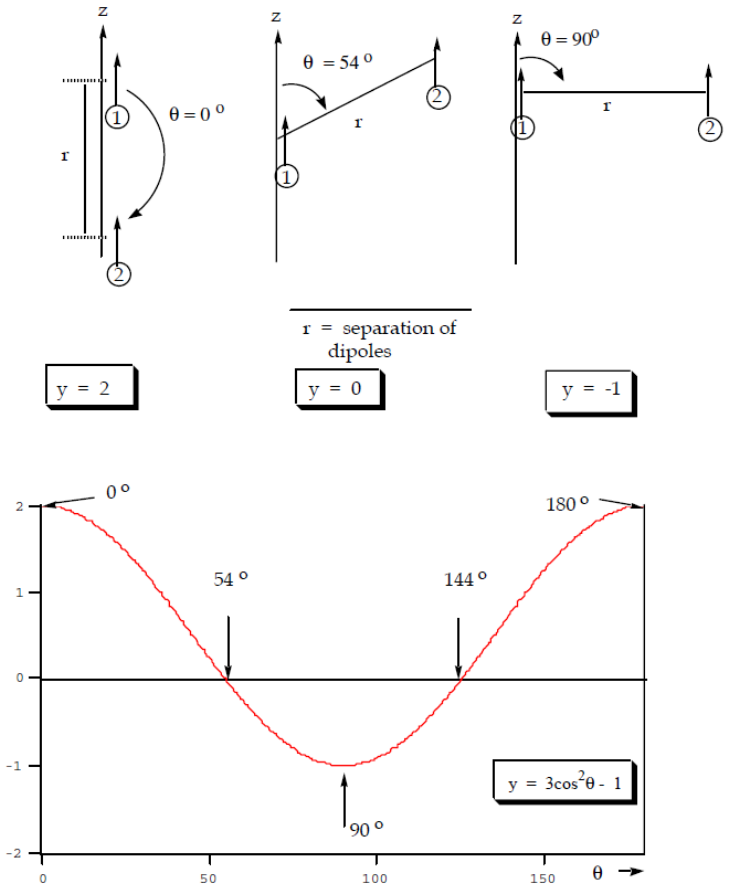

Figure 1.2 Dipole-dipole interactions of parallel magnetic moments. Top: vector representation of dipoles interacting at a fixed separation, r, and various orientations relative to the z-axis. Bottom: plot of the value of $y = 3\cos^2\theta - 1$ as a function of θ. [30]

Dipolar interactions are of particular importance for the rare-earth ions due to their high magnetic moment value. The dipolar interaction energy (D_{nn}) between two magnetic moments can be expressed as

$$D_{nn} = \frac{\mu_o}{4\pi r_{nn}^3}\left[\mu_1.\mu_2 - \frac{3}{r_{nn}{}^2}(\mu_1.r_{nn})(\mu_2.r_{nn})\right] \quad (1.1)$$

(μ_1 and μ_2 are two magnetic dipoles separated by distance r_{nn}). The strength of the interaction is proportional to several factors, namely, the magnitude, separation, and orientation of individual interacting dipoles and the "spectral overlap" of resonances that satisfy the conservation of angular momentum and energy [29].

The magnetic dipolar interaction is too weak to be accounted for its contribution in long-range ordering for materials having an ordering temperature of the order of 1000 K or so, however for systems developing order in milliKelvin temperature range and having large magnetic moments (~ 10 μ_B), these interactions play a crucial role in determining the magnetic ground state.

1.2.2 Exchange Interaction

Exchange interaction is an electrostatic interaction playing an elemental role for the occurrence of long-range ordering. It is a quantum mechanical phenomenon that arises between identical particles. The types of exchange interactions can be classified as follows:

Direct Exchange Interaction

The Hamiltonian for direct exchange interaction, based on the Heisenberg model, can be expressed as

$$H = -\sum_{ij} J_{ij}\, S_i.\, S_j \quad (1.2)$$

where J_{ij} is the exchange constant between the i^{th} and j^{th} spins. S_i and S_j are the spin magnetic moment at the i^{th} and j^{th} atomic sites. If J_{ij} is positive, for the system to have minimum energy, S_i and S_j must be parallel ($\cos 0° = 1$), and hence the material is ferromagnetic, and vice-versa J_{ij} is negative for antiferromagnetic systems.

Exchange interactions are simply electrostatic interactions and crucial to be considered for long-range magnetic ordering. The measure of this exchange energy is provided by the Weiss constant, θ_{CW}, which appears in the Curie-Weiss law,

$$\chi = C / (T - \theta_{CW}) \tag{1.3}$$

From the mean-field theory, it is shown that

$$\theta_{CW} = 2S(S+1)/3k \sum z_n J_n \tag{1.4}$$

where n is the n^{th} neighbor and J_n, the corresponding exchange constant. θ_{CW} is the algebraic sum of all the exchange interactions in any magnetic system, and thus the Curie-Weiss constant is the measure of the energy scale for the magnetic interactions [31], [32]. In the absence of frustrated magnetic materials, a strong deviation is expected from the Curie-Weiss law for $T \sim \theta_{CW}$.

Origin of exchange interaction: The origin of the exchange interaction can be understood by the effective overlap of the wave function for two electrons with spatial coordinates $\mathbf{r_1}$ and $\mathbf{r_2}$ whose joint state could be written as $\psi_a(\mathbf{r_1}) \bullet \psi_b(\mathbf{r_2})$; where $\psi_a(\mathbf{r_1})$ is the state of the first electron and $\psi_b(\mathbf{r_2})$ is the state of the second electron. However, this product does not obey exchange symmetry. The symmetrized and antisymmetrized wave function for the singlet Ψ_S and triplet Ψ_T state could be written as:

$$\Psi_S = 1/\sqrt{2}\ [\psi_a(\mathbf{r_1}) \bullet \psi_b(\mathbf{r_2}) + \psi_a(\mathbf{r_2}) \bullet \psi_b(\mathbf{r_1})]\ \chi_S \quad (1.5)$$

$$\Psi_T = 1/\sqrt{2}\ [\psi_a(\mathbf{r_1}) \bullet \psi_b(\mathbf{r_2}) - \psi_a(\mathbf{r_2}) \bullet \psi_b(\mathbf{r_1})]\ \chi_T \quad (1.6)$$

where both the spatial and spin parts of the wave function are included. The energies of the two possible states are

$$E_S = \int \Psi_S^* \hat{H} \Psi_S \mathrm{d}r_1 \mathrm{d}r_2 \quad (1.7)$$

$$E_T = \int \Psi_T^* \hat{H} \Psi_T \mathrm{d}r_1 \mathrm{d}r_2. \quad (1.8)$$

with the assumption that the spin parts of the wave function χ_S and χ_T are normalized. $\hat{H}$ is the Hamiltonian for an electron in an atom given as below

$$\hat{H} = \frac{1}{2m_e}(p + eA)^2 + 2\mu_B S.B + V(r) \quad (1.9)$$

where p is the momentum of the electron, the external magnetic field added is given as $\nabla \times A$, the energy of an electron in a magnetic field is given in terms of B as $E = g\mu_B m_s B$, V is the potential energy for the electron.

The difference between the two energies is

$$E_S - E_T = 2\int \Psi_a^*(r_1)\ \Psi_b^*(r_2)\ \hat{H} \Psi_a(r_2)\ \Psi_b(r_1)\ \mathrm{d}r_1 \mathrm{d}r_2 \quad (1.10)$$

For a singlet pair $S_1.S_2 = -3/4$ while for a triplet pair $S_1.S_2 = 1/4$. Hence the Hamiltonian can be written in the form of an "effective Hamiltonian".

$$\hat{H} = 1/4(E_S + 3E_T) - (E_S - E_T)\ S_1.S_2 \quad (1.11)$$

This is the sum of a constant term and a term that depends on the spin. The constant can be absorbed into other constant, but the second term is much interesting. The exchange constant (or exchange integral), J, is defined by

$$J = \frac{E_S - E_T}{2} = \int \Psi_a^*(r_1)\ \Psi_b^*(r_2)\ \hat{H}\Psi_a(r_2)\ \Psi_b(r_1)\ dr_1 dr_2 \quad (1.12)$$

And hence the spin-dependent term in the effective Hamiltonian can be written as

$$\hat{H}^{spin} = -2J\ S_1.S_2 \quad (1.13)$$

If $J > 0$, $E_S > E_T$ and the triplet state S = 1 is favored. If $J < 0$, $E_S < E_T$ and the singlet state S = 0 is favored. This equation is relatively simple to derive for two electrons; however, generalizing it to a many-body system is far from trivial. The Hamiltonian of the Heisenberg model is written as:

$$\hat{H} = -\sum_{ij} J_{ij} S_i.S_j \quad (1.14)$$

Where J_{ij} is the exchange constant between the i^{th} and j^{th} spins, factor 2 is omitted to exclude double counting between each pair of spins [29].

The true exchange interaction within the individual cations is the Coulomb repulsion of the charge overlap given by [33]

$$V_{ex}^{in} = \tfrac{1}{2} \sum_{R,n\neq n',\sigma\neq\sigma'} J_{nn'}\ s_{n'}^*(R,\sigma') \times s_n^*(R,\sigma)\ s_{n'}(R,\sigma)\ s_n(R,\sigma'), \quad (1.15)$$

where,

$$J_{nn'} = \int dr \int dr'\ f_n^*(r)\ f_{n'}(r) \times f_{n'}^*(r')\ f_n(r')\ e^2 |r-r^i|^{-1} \quad (1.16)$$

is the exchange integral. The part of this which leads to spin polarization is that in which electron r' goes from the d-band to an empty one, while electron r goes from a full band into the d- band; f denotes normally full bands, σ is spin and s^n's are the spin vector associated with state *n*.

Indirect Exchange Interaction (Superexchange Interaction)

Direct exchange refers to the interaction between neighboring moments, but in superexchange interaction, the coupling between two nearest-neighbor cations occurs via a shared nonmagnetic ion (e.g., oxygen). In the case of rare-earth metal oxides, such as in pyrochlore systems, the hybridization occurs between the rare-earths 4f-orbital and the O's 2p orbital. In such systems, since the rare earth's 4f orbital is strongly shielded by its fully filled 5s, 5p, and 5d orbital, the possibility of superexchange interaction is too weak to be considered [29].

Anisotropic exchange interaction (Dzyaloshinskii-Moriya; D.M.)

Here, the spin-orbit interaction plays the same role as the oxygen atom in superexchange. The Dzyaloshinskii-Moriya (D.M.) interaction is a process in which the excited state is not connected with oxygen as in the case of superexchange interaction but is originated by the spin-orbit interaction in one of the magnetic ions. An exchange interaction occurs between the excited state of a magnetic ion and the ground state of the neighboring ion. This type of interaction is called as Dzyaloshinskii-Moriya (D.M.) interaction or anisotropic exchange interaction. When this type of interaction is present between spins S_i and S_j, it is given in the form of a new term in the Hamiltonian as [29]

$$H_{DM} = D \cdot (S_i \times S_j) \tag{1.17}$$

Since we are concerned with low-temperature spin dynamics, the interaction between ground and excited state electrons is ruled out; hence this interaction has no role in the case of low-temperature spin dynamics of pyrochlores.

1.3 Magnetic frustrations

Despite having an ordered crystallographic arrangement, many systems possess disordered spin configurations due to the outcome of "competing interactions" and display different possible characteristic spatial correlations depending upon the dominating interactions between pairs of interacting magnetic degrees of freedom. Overall, these are the ensembles of interacting components, which cannot settle into a state that minimizes each interaction. The ratio of the Curie-Weiss temperature and the magnetic ordering temperature can be parameterized as a frustration index given as [23]:

$$f = |\theta_{CW}|/T_{N,C} \tag{1.18}$$

Geometrical frustration occurs in a magnetic system when the spatial arrangement of the magnetic moments ("spins") combined with their specific effective near neighbor interactions J_{eff} inhibits the formation of a 'simple' ordered collinear ground state at low temperatures at $T \leq J_{eff}$. As a result of the frustration, e.g., $Y_2Mo_2O_7$ lacks long-range ordering, and the spins show glass-like freezing, whereas, in $Tb_2Ti_2O_7$, spins remain dynamic even down to the lowest accessible temperatures. Some systems, e.g., $Gd_2Ti_2O_7$, TbNiAl, and $CsCoBr_3$, dynamic (paramagnetic) spins coexist with ordered spins, even at a temperature considerably lower than the Curie-Weiss temperature [34], [35] . The spin ordering pattern in these systems often shows signs of frustration. [22], [36].

This entails that not only one or a few classical spin configurations in the material minimize the energy, but instead, the number of ground states is extensively large, inducing highly entangled states if quantum effects play a significant role. All are transition metal oxides that crystallize with magnetic lattices that are geometrically or topologically prone to frustration

are based on spins with antiferromagnetic (AFM) coupling to nearest neighbor triangles or tetrahedra which share corners, edges, or faces. The phenomenon of geometric magnetic frustration in the context of several key materials is discussed below:

1.3.1 Frustration in two-dimension

The terms "order" and "disorder" can be defined in the realm of magnetism on a spin level, where "spin" corresponds to the orientation of magnetic moments caused by atoms in a compound. Both the ferromagnetic and antiferromagnetic coupled Ising type spins have been compared on the vertices of a square lattice to understand the phenomenon of frustration, as shown in **Figure 1.3 (a).** For ferromagnetically coupled spins, the system is in the disordered paramagnetic phase for high temperatures. Below a critical temperature T_c, the spins get ordered and take one of the ground states, where all spins follow a parallel ordering according to the ferromagnetic coupling. The minimum energy state results in a single spin configuration, where the Ising spins are along the positive or negative direction to a given axis. Similar is the case for AFM interaction between the nearest neighbors on the square lattice, as shown in **Figure 1.3 (b)**, below the critical temperature T_N. Both types of the spin correlation result in a non-frustrated system [31].

Similarly, if we consider FM interaction between the spins on the vertices of a triangular lattice, the interaction will result in an unfrustrated system, as shown in **Figure 1.4 (a).** The Hamiltonian, considering the interaction between any two spins, can be written as a scalar product of the spin operators [31],

$$H_{ex} \sim -2J_{ij}\, S_i .\, Sj \qquad (1.18)$$

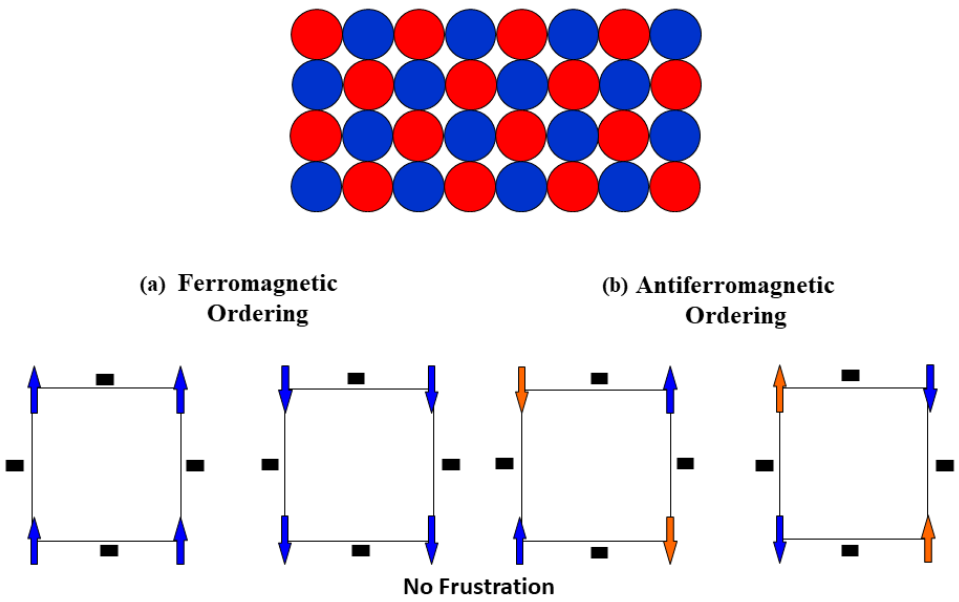

Figure 1.3 (a) Ferromagnetic and (b) antiferromagnetic Ising type spins on the vertices of a square lattice. Both types of spin coupling on this lattice site result in an unfrustrated system.

By convention for FM interaction, J_{ij} is positive; hence for up or down alignments between all spin pairs ($\theta = 0^{\circ}$; $\cos\theta = 1$; $H_{ex} = -2J_{ij}$), the energy is minimized between all the three spin pairs. The canonical example of 2D frustration is antiferromagnetically coupled Ising-like spins upon a regular triangular lattice shown in **Figure 1.4 (b).**

J_{ij} is negative, for antiferromagnetic (antiparallel) correlation between Ising spins and J_{ij} is equal for all nearest-neighbor pairs at the vertices of an equilateral triangular "plaquette". Under this condition, energy minimization is possible for only two of the three spin pairs since constraints set by AFM coupling cannot be satisfied simultaneously for all three spin-pairs, i.e., the system is geometrically frustrated. If we consider pairwise interaction, two parallel spin pairs result in a minimum energy value of -2J, but the third spin pair ends up with an exchange energy of +2J as explained:

$$H_{ex} \sim -2J\, S_1.S_2 \; (\theta = 0^{\circ};\ \cos\theta = 1;\ H_{ex} = -2J \tag{1.19}$$

$$\theta = 180^{\circ};\ \cos\theta = -1;\ H_{ex} = +2J) \tag{1.20}$$

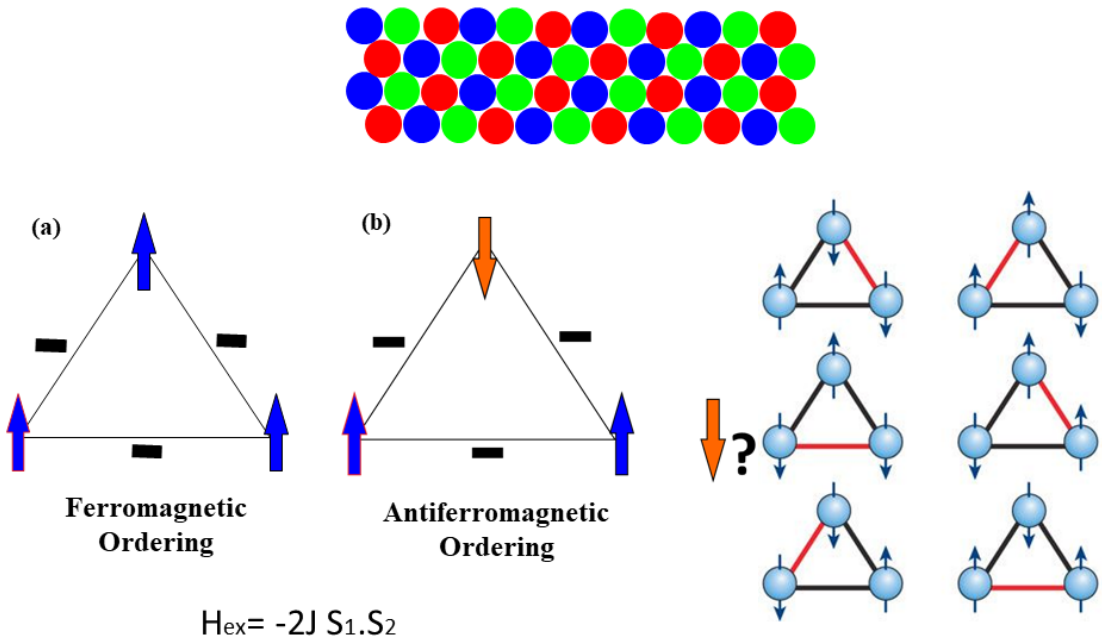

Figure 1.4 (a) Ferromagnetic and (b) antiferromagnetic interaction between the spins on the vertices of a triangular lattice.[37]

The second 2D example of a frustrated lattice is a situation for the square planar plaquette, as shown in **Figure 1.5.**

This system is clearly unfrustrated under the constraints of $J_{nn} >> J_{nnn}$ or $J_{nn} << J_{nnn}$, where J_{nn} is the interaction between the nearest neighbor spins and J_{nnn}, the next nearest neighbor spins (along the diagonal). This lattice can also be rendered frustrated for the special case of $J_{nn} \sim J_{nnn}$ and with antiferromagnetic spin coupling.

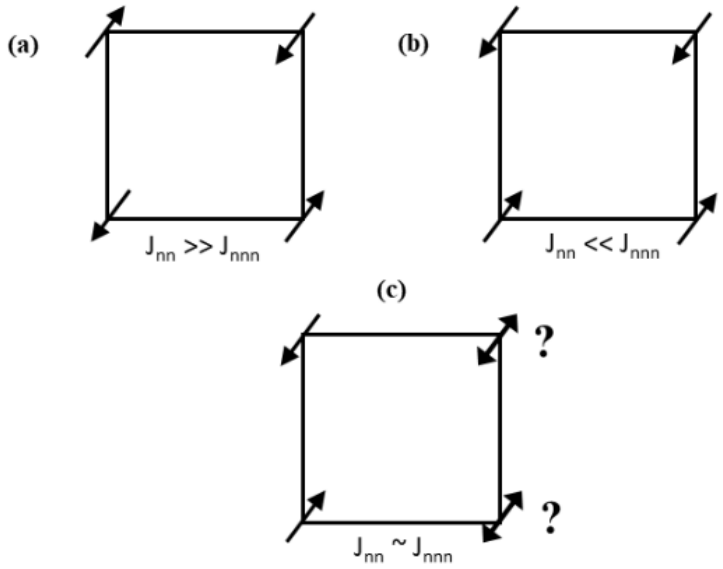

Figure 1.5 (a) $J_{nn} >> J_{nnn}$ and (b) $J_{nn} << J_{nnn}$ condition on a square lattice site result in an unfrustrated system, whereas (c) $J_{nn} \sim J_{nnn}$ ends up with frustrated "plaquettes" of a square planar lattice. [31]

Two well-known geometrically frustrated 2D frustrated lattices are corner-sharing triangles (Kagome lattice) and edge-sharing triangular lattices, as shown in **Figure 1.6** [31]**.**

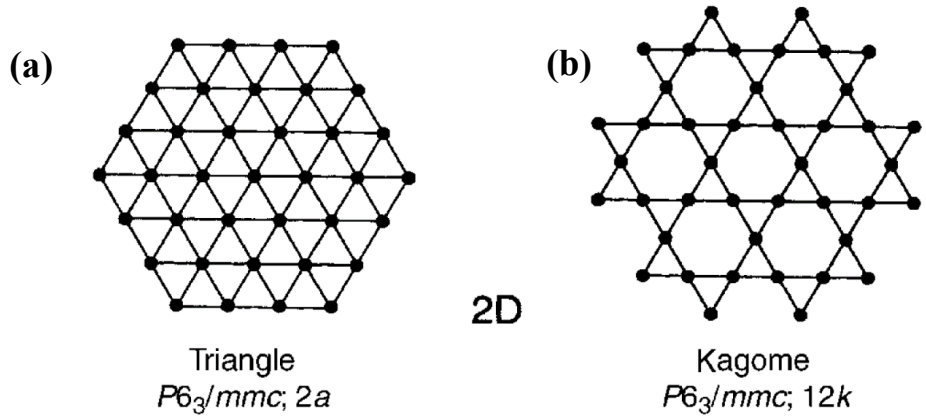

Figure 1.6 (a) Edge-sharing and (b) Corner-sharing (Kagome) triangular lattices having disordered spin arrangement. [31]

1.3.2 Frustration in three-dimension

The three-dimensional frustrated systems are much more complicated since their dimensionality makes a microscopic investigation difficult, thus making it an exciting and challenging field of research. The simplest example of 3D frustration could be considered where spins are antiferromagnetically coupled on a tetrahedral lattice, which is four edge-sharing equilateral triangles. Here, 1/2 of the spin sites are frustrated, as shown in **Figure 1.7 (a)**. The array of such spin arrangement results in the most important three-dimensional frustrated materials, as shown in **Figure 1.7 (b)** for a pyrochlore lattice. It consists of alternating Kagome and triangular planar layers stacked along a <111> direction, as represented in **Figure 1.7 (c)** [18]**.**

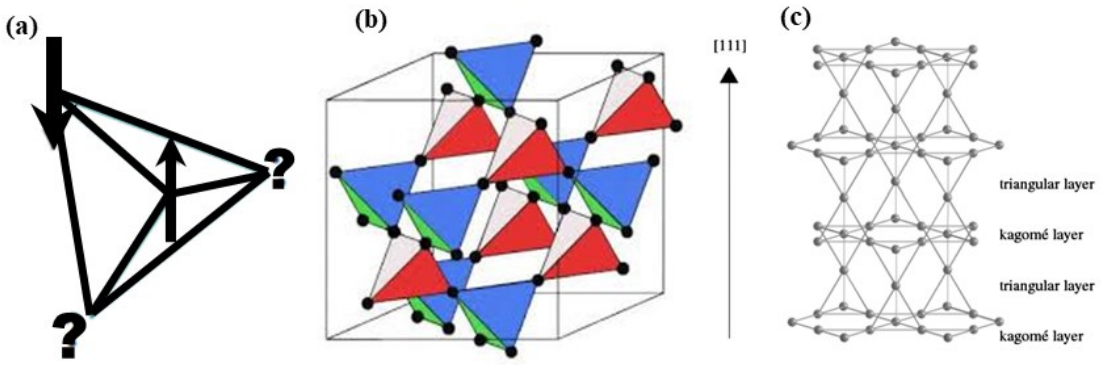

Figure 1.7 (a) The simplest example of 3D frustration is antiferromagnetically coupled spin on the vertices of a tetrahedral lattice. (b) The array of such spin arrangements within the lattice constitutes the frustrated pyrochlore lattice. (c) The pyrochlore lattice consists of an alternating kagome and triangular planar layers stacked along a <111> direction. [18], [31]

Such magnetically frustrated systems are supposed to be the ideal candidates for the emergence of novel exotic magnetic ground states since they exhibit large quantum

mechanical spin fluctuations. Short-range local spin orientation decides the magnetic properties that display new physics in different temperature regimes. Such a spin configuration is easily realized in case of pyrochlores, which is discussed as follows.

1.4 Pyrochlore lattice

It has become almost synonymous to refer to the lattice of corner-sharing tetrahedra as pyrochlore lattice since the mid-1980s. The name pyrochlore has been derived from the mineral $NaCaNb_2O_6F$. Most of the pyrochlore oxides crystallize in the space group ($Fd\bar{3}m$) having a cubic structure with general molecular formula $A_2B_2O_7$ (A = rare earth metal ion; B = d block transition metal ion). In cubic pyrochlores, A and B ions reside on two distinct interpenetrating corner-sharing tetrahedral sublattices, as could be seen from **Figure 1.8** [18].

To formulate the structural setting, i.e., crystallographic orientation, the preferable formula is $A_2B_2O_6O'$. According to the International tables of crystallography, the Wyckoff positions, point symmetry, and minimal coordinates suitable for these cubic pyrochlores with origin at 16c are:

Atom	Wyckoff positions	Point symmetry	Minimal coordinates
A	16d	$\bar{3}m$ (D_{3d})	(1/2,1/2,1/2)
B	16c	$\bar{3}m$ (D_{3d})	(0,0,0)
O	48f	mm (C_{2v})	(x,1/8,1/8)
O'	8b	$\bar{4}3m$ (T_d)	(3/8,3/8,3/8)

The local atomic arrangement is shown in **Figure 1.9.** The coordination geometry about the metal sites is controlled by the value of *x,* which is the variable positional parameter for the oxygen atom at the 48f Wyckoff site. For the value of x = 0.3125, perfect octahedron results about B site (16c) and for x = 0.375, perfect cube results about A site (16d).

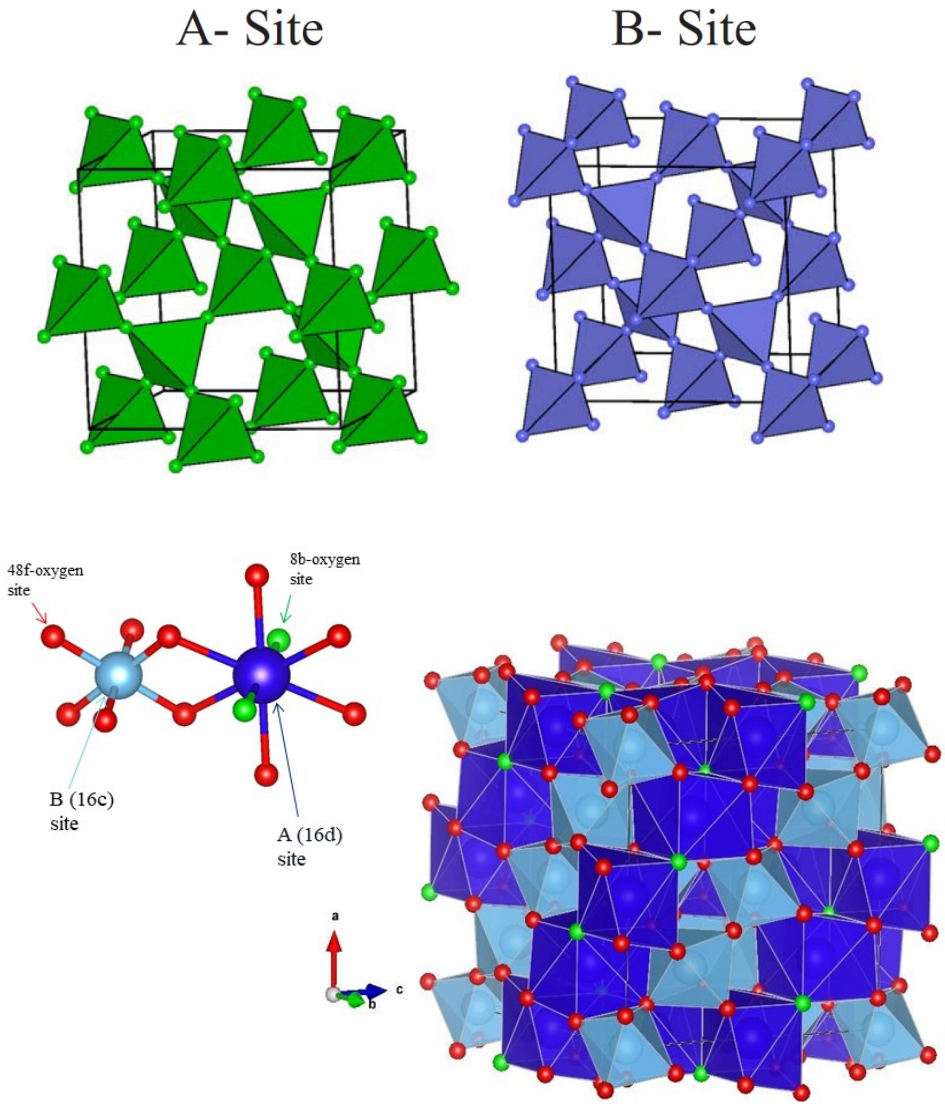

Figure 1.8 (Top) Cubic pyrochlores ($A_2B_2O_7$; A = rare earth metal ion & B= d block transition metal ion) with A and B ions residing on two distinct interpenetrating corner-sharing tetrahedral sublattices. (Bottom) Three-dimensional pyrochlore lattice along with the Wyckoff sites assigned to these atomic positions according to the International tables of crystallography. [18]

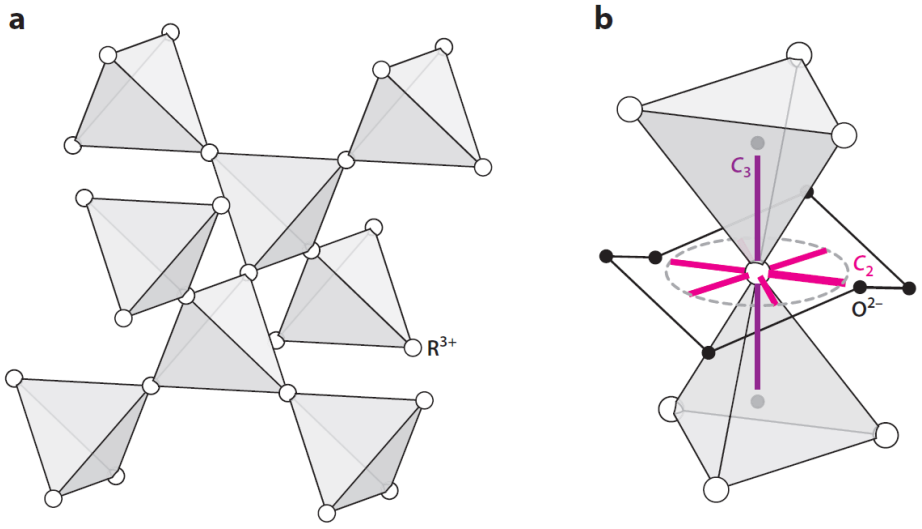

Figure 1.9 (a) Crystal structure of the magnetic ions in the rare-earth pyrochlores. (b) Local environment of a rare-earth ion showing the surrounding oxygen ions. The local *XY* plane of the ion, as well as the C_2 and C_3 rotation axes of the D_{3d} site symmetry group. [11]

For a typical pyrochlore, the distortion about the B site ion or 16c site is minor.

- The $\bar{3}$m symmetry means all 6 B-O bonds are of equal lengths.
- The O-B-O angles are distorted only slightly from ideal octahedral values of 90° having values lying between (81-100) °.
- The distortion of A site geometry from the ideal cube is very large.
- A-O and A-O' bond distances are different: A-O = (2.4-2.5) Å and A-O' = 2.2 Å.

The pyrochlore structure can be described as two interpenetrating networks, one of the compositions B_2O_6, which is a network of corner-sharing metal-oxygen octahedral (equivalent to perovskite structure) and the other of composition A_2O' which forms a zigzag chain through the channels formed by B_2O_6 network. The only Ising-like anisotropy consistent with this

symmetry is that the easy axes point along the cubic <111> directions into the centre of the tetrahedron. The antiferromagnetic ground state for the pyrochlore lattice is unique, consisting of alternate tetrahedra with four spins 'in' or four spins 'out'.

1.4.1 Magnetic interactions in specific to Pyrochlore Lattice

The interaction Hamiltonian applicable to a magnetically frustrated pyrochlore system with $Fd\bar{3}m$ space group can be written as [38]:

$$H = H_{cf}\,(\text{crystal field interaction}) + H_{int}\,(\text{spin-spin interactions}) \qquad (1.21)$$

H_{cf} is fixed by the symmetry of the magnetic ion environment and is discussed later. H_{int} constitutes the exchange (H_{ex}) and dipolar (H_{dp}) interaction Hamiltonian ($H_{int} = H_{dp} + H_{ex}$). H_{ex} can further be elaborated as consisting of four nearest-neighbor interactions, namely:

$$H_{ex} = H_{Ising} + H_{iso}\,(\text{isotropic exchange}) + H_{pd}\,(\text{pseudo dipolar}) + H_{DM}\,(\text{Dzyaloshinskii-Moriya}) \qquad (1.22)$$

These exchange interactions can further be expressed as:

$$H_{Ising} = -J_{Ising} \sum_{<i,a;j,b>} (J_i^a \cdot \hat{z}^a)(J_j^b \cdot \hat{z}^b) \qquad (1.23)$$

$$H_{Heisenberg} = -J_{Heisenberg} \sum_{<i,a;j,b>} J_i^a \cdot J_j^b \qquad (1.24)$$

H_{Ising} couples the local [111] z component of J for Ising spins, whereas H_{iso} accounts for the standard isotropic exchange interaction between the spins.

$$H_{pd} = -J_{pd} \sum_{<i,a;j,b>} (J_i^a \cdot J_j^b - 3(J_i^a \cdot \hat{R}_{ij}^{ab})(J_j^b \cdot \hat{R}_{ij}^{ab})) \qquad (1.25)$$

This is a type of pseudo-dipolar exchange interaction having its origin in exchange interaction. Last is the $H_{DM,}$ which considers the anisotropic exchange interaction between two magnetic

spins and can be expressed as:

$$H_{DM} = -J_{DM} \sum_{<i,a;j,b>} \Omega_{DM}^{a,b} . (J_i^a \times J_j^b) \quad (1.26)$$

J_{Ising}, $J_{Heisenberg}$, J_{pd}, and J_{DM} are the exchange terms for nearest-neighbor interactions and can altogether be accounted into the overall exchange term J_{ex}.

Magnetostatic dipolar interaction can further be expressed as

$$H_{dp} = \frac{1}{2} \sum_{<i,a;j,b>} \frac{(D_{nn})^3}{\left|R_{ij}^{ab}\right|^3} (J_i^a . J_j^b - 3(J_i^a . \hat{R}_{ij}^{ab})(J_j^b . \hat{R}_{ij}^{ab})) \quad (1.27)$$

where J_i^a denotes the angular momentum of the rare earth ion at R_i^a lattice site (FCC lattice site *i,* and tetrahedral sublattice site *a*). $\hat{R}_{ij}^{ab}$ is a unit vector directed along $R_j^b - R_i^a$ [38]. The simplified version of this interaction Hamiltonian applicable to the Dipolar spin-ice model is discussed in section 1.9.

1.5 Spin ice

Ever since the discovery of $Ho_2Ti_2O_7$ and $Dy_2Ti_2O_7$ as a topologically frustrated ferromagnet, it has fascinated researchers to investigate it in detail. A mean-field theory calculation of the Heisenberg Hamiltonian provided indirect confirmation of two (out of four) branches of exactly degenerate soft (critical) modes throughout the Brillouin zone, i.e., no unique state develops long-range order at the mean-field critical temperature [39], [40]. Spin-ice phenomenon in pyrochlore oxide materials – where Ising like magnetic moments of rare-earth (Ho^{3+}/Dy^{3+}) occupy a lattice of corner shared tetrahedron and are coupled by ferromagnetic (dipolar) interaction. Each tetrahedron of (Ho^{3+}/Dy^{3+}) ions have an O^{2-} ion at its centre, two of O^{2-} ions lie close to each (Ho^{3+}/Dy^{3+}) along the <111> crystallographic axis, which

connects the centre of the tetrahedron to its vertex. The system possesses a number of quasi degenerate ground spin states and displays a low-temperature entropy, equivalent to the proton disorder entropy of water ice; hence called spin ice. The anisotropic crystallographic environment changes the quantum ground state of (Ho^{3+}/Dy^{3+}) such that its magnetic moment vector has its maximum possible magnitude and lies parallel to the local <111> axis. In the language of quantum mechanics, for $Ho_2Ti_2O_7$ spin-ice, the $^5I_8$ free ion ground state is split by the local trigonal crystal field such that the ground state is an almost pure $|J, M_J\rangle = |8, \pm 8\rangle$ doublet with <111> quantization axis, thus making it an Ising spin configuration.

1.6 Spin relaxation apart from spin-ice in different spin frustrated systems

1.6.1 Unconventional long-range ordering

Another magnetically frustrated system, $Gd_2Ti_2O_7$, follows the Curie-Weiss law till ~ 10 K with the value of θ_{CW} = -9.6 K, as shown in **Figure 1.10 (a)** [41] [42]. From dc-susceptibility, there is no evidence of magnetic ordering down to ~ 1 K. But specific heat data suggests unequivocal evidence for a phase transition to long-range ordering shown in **Figure 1.10 (b)**[42]. The said measurement exhibit two such transitions at 0.97 K and 0.7 K in the absence of an external magnetic field. Additional transitions are induced at an applied magnetic field. The explanations of this ordered state at zero field have been inferred through neutron scattering. In the study at 50 mK at a spallation source, a k = (1/2,1/2,1/2) structure was found, as shown in **Figure 1.11 (a).** This structure is associated with a very unusual and unexpected spin configuration, in which 3/4th of the Gd^{3+} spins are ordered within the Kagome planes, while 1/4th of the spins related to interplanar sites remain disordered.

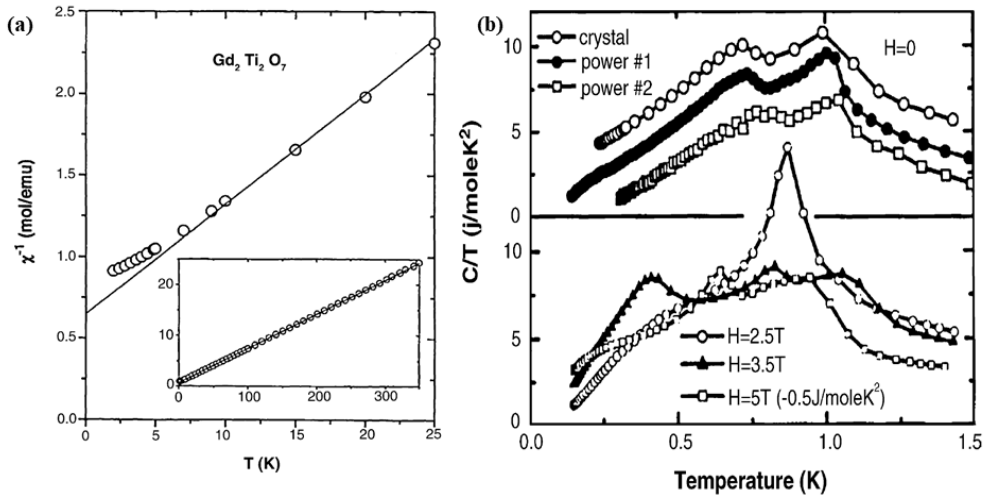

Figure 1.10 (a) dc-susceptibility data for $Gd_2Ti_2O_7$ showing Curie–Weiss behavior at T ~10 K and no sign of long-range order till T ~1 K. (b) Presence of two-phase transitions at 0.9 and 0.7 K (zero applied field) from heat capacity data on $Gd_2Ti_2O_7$ (top). Induction of new transitions in applied fields (bottom). [42]

Such a structure has been termed as the single or 1 k structure. A new (1/2,1/2,1/2) magnetic reflection was also found later and modified the picture.

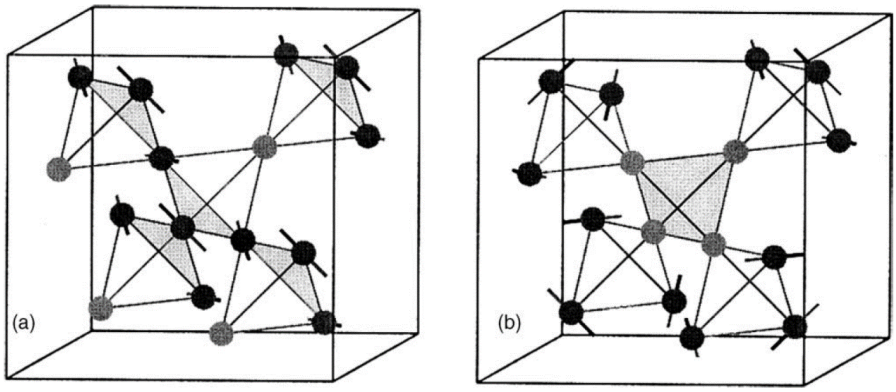

Figure 1.11 (a) The 1 k magnetic structure for $Gd_2Ti_2O_7$, which is consistent with the neutron diffraction data above 0.7K. (b) The 4k magnetic structure of $Gd_2Ti_2O_7$ consistent with both the Bragg and diffuse neutron diffraction data below 0.7 K. The dark spheres represent Gd ions with a full (7.0μ_B) ordered moment while the grey spheres carry only a 1.9 μ_B ordered moment. [42]

This Bragg peak can give a finite intensity only if the interplanar sites are also ordered. It appears below 0.7 K, which corresponds to the lower phase transition as seen in the specific heat measurements. The intensity analysis of this reflection indicates that only partial order (~27%) is present on these sites, and a significant diffuse component is seen at Q = 1.1 A, indicating that the correlation length of the disordered spins is ~3.5 Å. This distance is equal to the nearest neighbor distance within the Kagome planes rather than ~7 Å, which corresponds to the distance between the triangular, interplanar sites. The ordered part can be described as a 4-k structure, as shown in **Figure 1.11 (b).**

1.6.2 XY antiferromagnetic (Long-range ordering via an order by disorder mechanism)

The XY pyrochlores $Er_2Ti_2O_7$ and $Yb_2Ti_2O_7$ have been investigated in details because in these compound quantum fluctuations play a major role in stabilizing the ground state and are providing insight into the prevalence of the so-called "order-by-disorder" mechanism in frustrated systems [43]. In the case of $Er_2Ti_2O_7$, a magnetic phase transition occurs at T_N = 1.2 K, as evidenced by a lambda-like feature in the specific heat, shown in **Figure 1.12 (a)**, and a cusp in the dc-susceptibility, as shown in **Figure 1.12 (b)** [44]**.** Early experiments on this material suggested that the ordered state, usually described by the irreducible representations ψ_2 or ψ_3, is selected by the quantum order-by-disorder mechanism. Within this scenario, quantum fluctuations drive the resulting spin configuration at low temperatures. The magnetic structure of this compound was inconclusive as the spin configuration belonging to ψ_2, and ψ_3 Irreps give virtually indistinguishable powder neutron diffraction pattern. Recent neutron polarimetry experiments, coupled with sophisticated numerical work

to model the thermodynamic properties within the ordered state, have verified that the non-coplanar ψ_2 state is indeed the likely magnetic structure and that order-by-disorder cannot be ignored as an essential ingredient of XY pyrochlore magnetism.

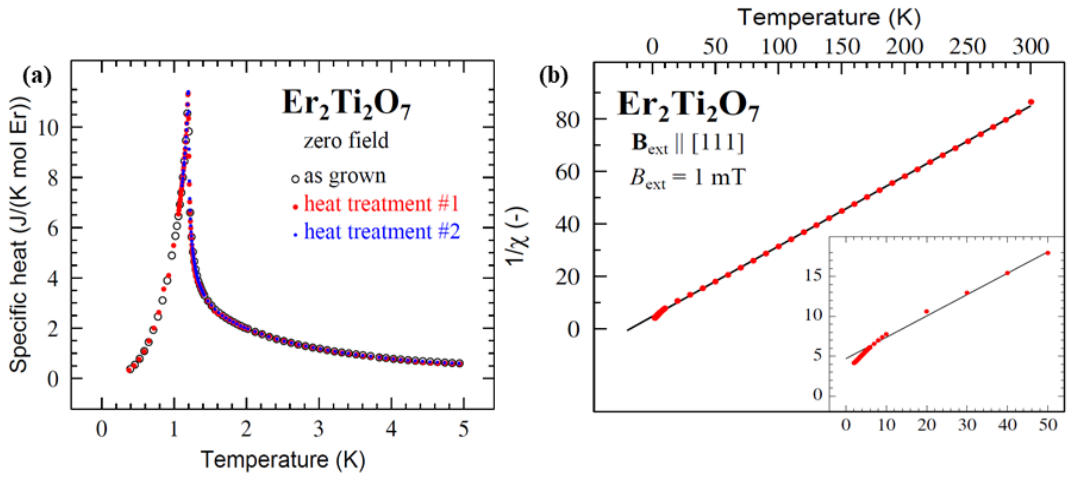

Figure 1.12 (a) Specific heat versus temperature for $Er_2Ti_2O_7$. (b) Inverse of the magnetic susceptibility of an $Er_2Ti_2O_7$ crystal versus temperature in a large temperature range. The solid line results from a fit with the Curie Weiss law. A field of 1 mT is applied along a diagonal of the cubic crystal structure. The inset shows the low-temperature range of the data. [44]

1.6.3 Spin Glass

Quenched random frustration is a major ingredient in a spin-glass type of material. In the spin-glass type of materials, there is a sudden transition to a glassy state of spins where the spins are quenched (frozen in time but random in direction) from the paramagnetic state of spins (having thermal fluctuations). The combination of randomness and frustration prevents the development of conventional long-range magnetic order characterized by delta-function magnetic Bragg peaks. The spins transit to a random frozen state from a randomly fluctuating state at spin freezing/glass (T_f/T_g) temperature. Magnetic interactions inhibit the development

of long-range magnetic ordering parameter. In that case, the molecular field produced by neighboring magnetic moments on each magnetic site is able to freeze the magnetic configuration at a characteristic temperature [45].

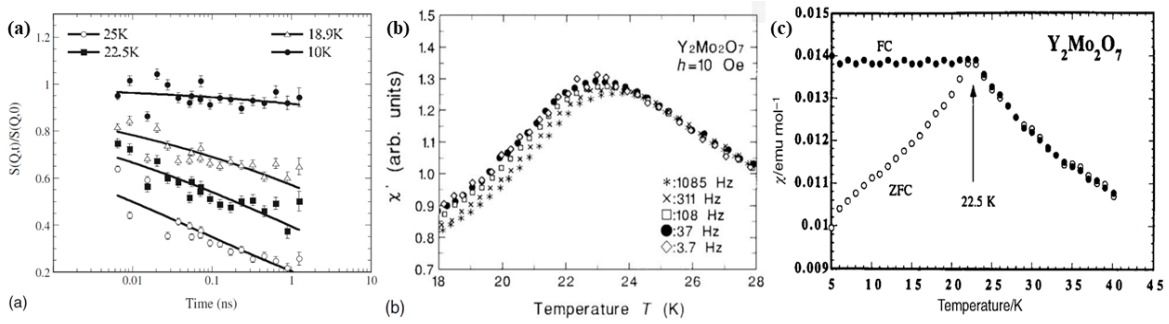

Figure 1.13 Spin dynamics in $Y_2Mo_2O_7$. (a) Neutron spin echo results for $Y_2Mo_2O_7$ at temperatures spanning Tf =22.5 K determined from static magnetization data. Note that within this time window, spin freezing is not fully established until 10 K. (b) Frequency-dependent ac susceptibility χ' for $Y_2Mo_2O_7$ showing classical spin-glass behavior. (c) dc-susceptibility showing T_f ~22.5 K. [18], [31]

Experimentally, a number of signatures are taken as an indicator of spin-glass state, such as the frequency dependence of χ' in the ac susceptibility, the linear temperature dependence of the low-temperature heat capacity, or the μSR line shape, but the definitive approach is measuring the temperature dependence of the nonlinear magnetic susceptibility. In the family of pyrochlores, the best evidence for the canonical spin-glass character came from the $Y_2Mo_2O_7$, which is reflected in the ac-susceptibility of at a nearly zero-field, which showed the classic frequency dependence as well as in the dc-susceptibility showing T_f ~ 22.5 K, as shown in **Figure 1.13** [18], [31]**.**

1.6.4 Spin liquid/Cooperative paramagnetism ($Tb_2Ti_2O_7$)

$Tb_2Ti_2O_7$ is an Ising pyrochlore system of a similar type to the Ho^{3+} and Dy^{3+} based materials, but the Ising anisotropy is reduced to a much lower temperature [46]. This makes the interpretation of experimental data more difficult, as initial estimates of the nearest-neighbor exchange and dipole moment yield $J_{nn}/D_{nn} \sim -1$, placing this system very close to the phase boundary of **Figure 1.1**. It is the same as co-operative paramagnetism and differs from spin glasses [27].

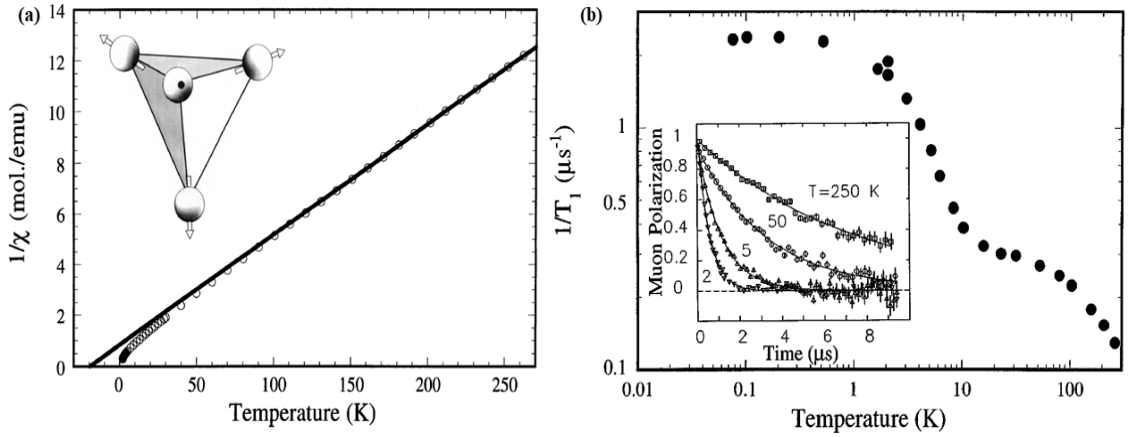

Figure 1.14 (a)The temperature dependence of the inverse susceptibility for $Tb_2Ti_2O_7$, along with a fit of the high-temperature regime of this data to a Curie-Weiss form. The inset shows the assumed local arrangement of moments on a single tetrahedron. (b) The variation with temperature of the muon spin relaxation rate for $Tb_2Ti_2O_7$ in a longitudinal applied field of 0.005 T. The inset shows the single exponential relaxation of the muon polarization at various temperatures. [47]

This has to lead to the labeling of this material as either a "co-operative paramagnet" (classical states) or a spin liquid (quantum states) [10]. There exists significant evidence, especially from neutron scattering, that strong magnetic correlations exist on a nearest neighbor length scale, ~ 5 Å, down to very low temperatures. Early reports of this compound indicated no

sign of magnetic ordering down to 57 mK, as evident by magnetic susceptibility (**Figure 1.14 (a)**), neutron scattering experiments, muon spin relaxation measurements (**Figure 1.14 (b)**), and heat capacity [47]. This is surprising given the strong antiferromagnetic exchange (θ_{CW} ~ −17.5(3) K) between the Ising-like spins of μ_{eff} = 9.6 μ_B. Strong magnetic diffuse scattering observed at low temperatures suggests that the spins in each tetrahedron are ordered as a local antiferromagnetic arrangement. However, these clusters are dynamic at low temperatures, yielding a "co-operative paramagnet" in the limit of 0 K. Many theories have been proposed for the low-temperature behavior of $Tb_2Ti_2O_7$, including those of a "quantum spin ice" state [48].

1.7 Spin ice: in the context of $Ho_2Ti_2O_7$

In "quantum spin ice" materials, quantum fluctuations nullify the possibility of any conventional long-range ordering down to the lowest possible temperature [13]. As a result of frustration, in $Ho_2Ti_2O_7$, spins lack long-range order and exhibits two distinct spin relaxation mechanisms, namely single ion freezing (T_s ~ 15 K) followed by ice like freezing (T_{ice} ~ 2 K). There are conflicting reports for these spin ordering being classical or quantum in nature [49]. Neutron Spin Echo (NSE) was performed to study the spin dynamics. Intermediate scattering function *S(q,t)* was measured to study the spatial and temporal correlation through *q* ($Å^{-1}$) and relaxation time *t* (s). **Figure 1.15** shows the normalized scattering function *S(q,t)* at different temperatures [36].

The spin relaxation *S(q,t)* is invariant of *q* for T = 74 and 100 K, is shown in the lower panel of **Figure 1.15.** At temperatures between 0.3 K and 200 K, the intermediate scattering function can be fitted with excellent precision to a simple exponential

$$\frac{S(q,t)}{S(q,0)} = A.\ \exp(-t/\tau(T)) \qquad (1.28)$$

where A = 0.91 ± 0.01 in the temperature range between ~ 2 K to 50 K. **Figure 1.16** shows the ac-susceptibility measurement of a single crystal of $Ho_2Ti_2O_7$ for an applied field of B =1 T [36].

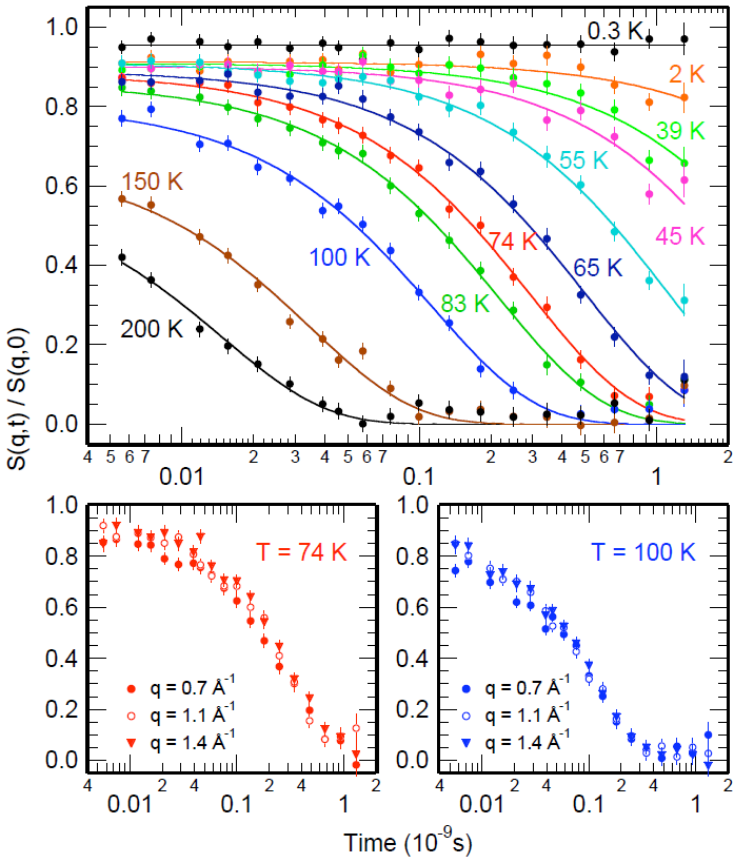

Figure 1.15 (Top panel) The normalized intermediate scattering function S(q, t)/S(q, 0) as measured through neutron scattering experiment, integrated in the range 0.5 °A^{-1} ≤ q ≤1.0 °A^{-1} at various temperatures. (Bottom panel) as a function of q, showing negligible q dependence. [36]

The feature at T_s ~15 K is seen at a high magnetic field, not in a low magnetic field, and the expected activation energy for this spin freezing is ~ 240 K. This peak was justified through NSE measurements too, which confirmed that T_s ~ 15 K relaxation is attributed to the

thermally activated single ion spin freezing process. But NSE measurement was not able to account for the Schottky anomaly at T~ 1K. Hence it was inferred from there that the lower temperature spin relaxation process might be related to quantum mechanical tunneling between two ground-state doublets.

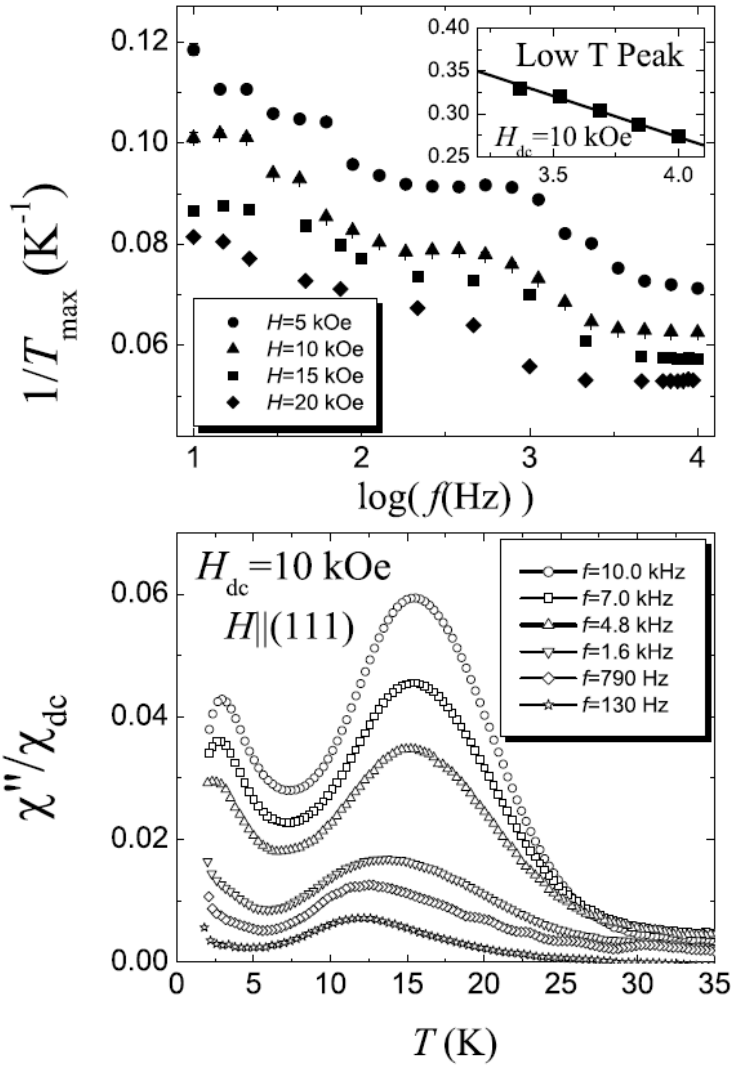

Figure 1.16 ac-susceptibility data taken on a single crystal of $Ho_2Ti_2O_7$. (Top) The high-temperature peak position as a function of log f at different fields. Inset: Arrhenius behavior of the low-temperature feature in the same field. (Bottom) Frequency dependence of the ac susceptibility (imaginary part) measured in an applied dc field B = 1 T parallel to the <111> axis. [36]

In another study of $Ho_2Ti_2O_7$, it was shown that strong local crystal field (CF) at D_{3d} (trigonal) site symmetry of Ho^{3+} results in the spin arrangement as almost ideal Ising spins along [111] direction (cubic three-fold symmetry axis) at $T_s \sim 15$ K (activation energy; $E_a \sim 20.6$ meV) [50], [51]. The crystalline electric field of $Ho_2Ti_2O_7$ is responsible for the splitting of the ionic states that leads to the phenomenon of frustration in this system. All the macroscopic degenerate states that follow "two in-two out" spin freezing arrangement (non-collinear disordered pattern) constitute the ground state of $Ho_2Ti_2O_7$ spin ice system. The transverse component of this effective field mixes the higher $|M_j>$ states with $|\pm 8>$ ground state doublet, facilitating the spin inversion by providing a number of degenerate spin configurations. Compared to other quantum magnets, in $Ho_2Ti_2O_7$, the spin relaxation mechanism presents much different scenario. Single ion process dominates over 15 K, while co-operative quantum tunneling phenomenon occurs over a much broader temperature range of T ~ 1-15K. This shows that $Ho_2Ti_2O_7$ can serve as a new class of quantum dynamical magnet. Within a narrow subspace, the highly anisotropic nature of exchange interaction can be varied to alter the Hamiltonian governing the spin dynamics. This alteration can manifest in several different ordered magnetic ground states relevant to rare-earth pyrochlores [16], leading to the varying magnetic states. Both J_{nn} and D_n plays a dominant role in deciding the effective exchange interaction "J_{eff}" and thus the low-temperature spin dynamics, which is indicated from the following expression [49]:

$$J_{eff} = \mu^2 S_i S_j (5D_{nn} - J_{nn}) /3 \qquad (1.29)$$

Hence, the interplay between these three (J_{nn}, D_{nn}, and CF) interactions at different energy and time scales decide the spin dynamics in $Ho_2Ti_2O_7$ in different temperature regimes.

The response of magnetization against temperature and magnetic field for $Ho_2Ti_2O_7$ is shown in **Figure 1.17** [27]**.** *M-T* measurement indicates that $Ho_2Ti_2O_7$ exhibits a soft magnetic behavior at low-*T* and a very sensitive magnetic response to an external magnetic field. This was further confirmed from the *M-H* hysteresis loop taken at *T*=2 K, which presents the soft ferromagnetic feature with a very small coercive field (H_c ~ 10 Oe) and magnetization becomes well saturated at *H* <10 kOe.

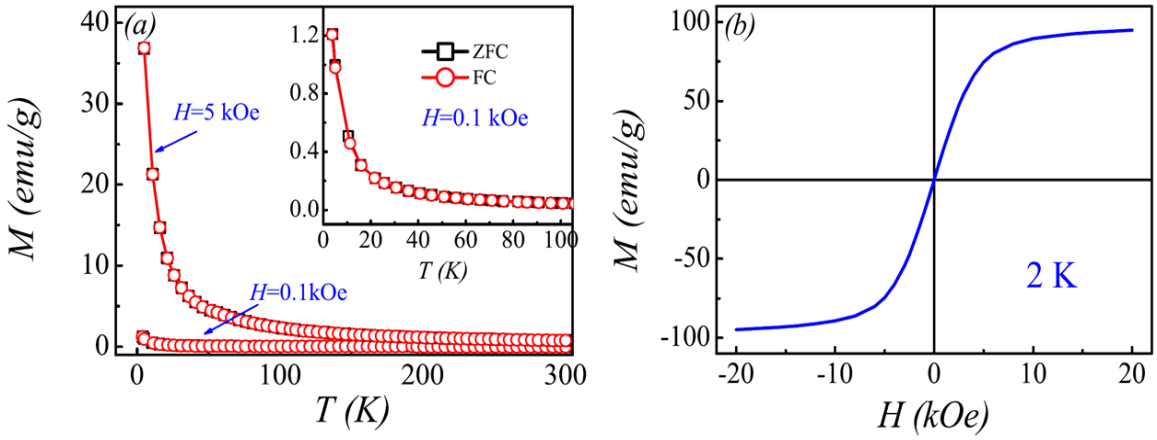

Figure 1.17 (a) The curves of M-T (magnetization vs. temperature) for both ZFC and FC sequences under the magnetic field H = 0.1 kOe and 5 kOe, respectively. The inset indicates the MT curves under H=0.1 kOe with the T-range of (2–100) K. (b) Magnetic hysteresis loop at 2 K in the H-range of (-20–20) kOe. [27]

The saturation magnetization is ~ 95 emu/g, i.e., 4.568 μ_B/Ho^{3+}, demonstrating that the Ho^{3+} spins are almost ferromagnetically aligned [27]. This sensitive response is usually favored for potential multiferroic applications along with the spin ice configuration of $Ho_2Ti_2O_7$. The other relevant measurements with provide evidence of lack of long-range ordering in $Ho_2Ti_2O_7$ is discussed as follows:

1.8 Experimental signatures of spin ice: [$(Dy/Ho)_2Ti_2O_7$]

In 1930, William Giauque and co-workers found that the limiting low-temperature state of hexagonal structure of ice as characterized by specific heat measurements results in non-vanishing entropy [42]. The value of this residual entropy had been determined to be S_0 = 1.68 J/mol. K, and no conventional origin for this could be traced. This was remarkable as it seemed to violate the third law of thermodynamics. The phenomenon was exposed by Linus Pauling, who traced it back to macroscopic proton (H^+) configurations and local hydrogen bonding of water molecules. In geometrically frustrated magnetic materials also, there exists an exponentially large number of degenerate classical ground states Ω. The N number of tetrahedra connected through the edge and corner-sharing form the entire pyrochlore sublattice, and the degeneracy of this lattice grows exponentially with the increase in the number of tetrahedra. The dependence is given by the formula $\Omega \sim (3/2)^{N,}$ where Ω is the number of degenerate states and N is the number of tetrahedra. This increase in the number of degenerate states results in residual entropy equivalent to S ~ R log(3/2) per mole tetrahedra, as estimated by Pauling in the case of water ice. The value of the residual, zero-point, or ground state entropy is $S= K_b \ln[3/2]$. For $Dy_2Ti_2O_7$, the behavior of residual entropy is clarified in **Figure 1.18** [53]. In the paramagnetic region temperatures, the magnetic moments follow Heisenberg's spin behavior, and all the sixteen microstates have equal probability. At lower temperatures, the spins freeze sequentially in 4-in or 4-out, followed by 3in/out:1out/in and finally at T ~ 2 K, “2 in-2 out” configuration.

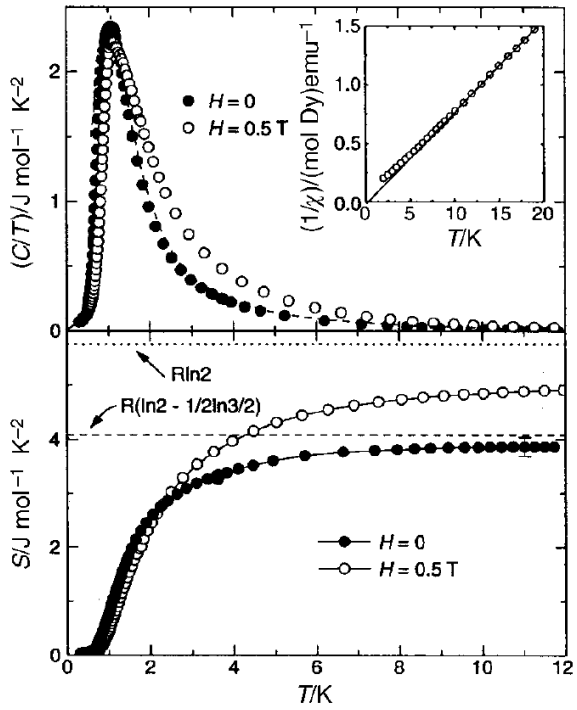

Figure 1.18 Limiting low-temperature state is characterized by a residual entropy, S = 1.68 J/mol. K known as zero point or residual entropy being observed in $Dy_2Ti_2O_7$. [53]

Figure 1.19 (a) shows the "2 in-2 out" orientation; the letter 6 in the bracket indicates six possible states [54]. Similarly, the "1 in-3 out" spin orientation, has eight degenerate states and "all in-all out" configuration have two states.

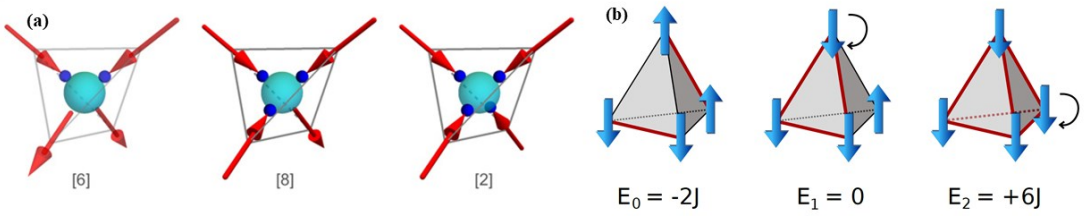

Figure 1.19 (a)"2 in-2 out" orientation, the letter 6 in bracket indicates six possible states. Adjacent to it is the "1 in-3 out" spin orientation, and this orientation has eight degenerate states. Last is the "all-in-all-out" configuration having two degenerate states. (b) Assigning an energy $+J_{eff}$ to an 'in–in' or 'out–out' pair and $-J_{eff}$ to an 'in-out' pair yields energies E (2:2) =$-2J_{eff}$, E (3:1) = 0 and E (4:4) = $+6J_{eff}$. [54]

The magnetic ground state in this system has the "two in-two out" spin arrangement. It is explained by assigning an energy $+J_{eff}$ to an 'in–in' or 'out–out' spin pair and $-J_{eff}$ to an 'in-out' spin pair, this yields energies $E(2:2) = -2J_{eff}$, $E(3:1) = 0$ and $E(4:4) = +6J_{eff}$ as shown in **Figure 1.19 (b)**. This confirms that the lowest possible energy state is exhibited by the spin-ice state, which is the ground state for $Ho_2Ti_2O_7$. The zero-field muon spin rotation measurement of $Ho_2Ti_2O_7$ at a temperature of 0.046 K and 4 K indicates no change in the initial symmetry or the decay rate over nearly two decades of temperatures. The similarity in the spectra at both temperatures suggests no change in spin dynamics, i.e., no phase transition over this temperature range, thus implying that $Ho_2Ti_2O_7$ lacks long-range ordering till a temperature as low as 0.046 K [55].

Figure 1.20 presents the neutron scattering measurement of $Ho_2Ti_2O_7$ in which the left panel suggests unusual temperature dependence of magnetic Bragg peak [56].

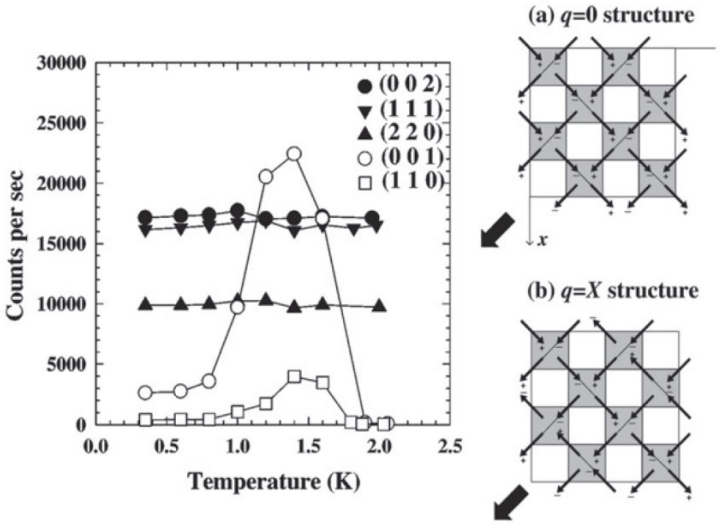

Figure 1.20 Neutron scattering data for $Ho_2Ti_2O_7$. (Left) Unusual temperature dependence of the magnetic Bragg peaks measured in an applied field of 2 T. (Right)The two sets of peaks (full and open circles) respectively suggest the q = 0 and q = X magnetic shown as (a) and (b). [54]

The solid circles represent scattering wave vector $q = 0$, and the open circles are q = X belonging to magnetic structures. For $q = X$, i.e., width varies with temperature, which again implies an incomplete correlation among the chain of spins perpendicular to the applied field (2 T). For $Ho_2Ti_2O_7$, dc-susceptibility measurement provided the value of $\theta_{CW} = +1.9 \pm 0.1$ K, indicating an intrinsically ferromagnetic spin correlation. It is obvious that FM system must order at $T = T_C$. Interestingly for $Ho_2Ti_2O_7$, J_{nn} is AFM, whereas the effective magnetic interaction (J_{eff}) is FM in nature as characterized by a positive θ_{CW} yet showing no signs of long-range magnetic ordering down to 50 mK [26]. Hence, despite having a positive θ_{CW} as shown in **Figure 1.21,** $Ho_2Ti_2O_7$ lacks long-range ordering as had been explained from the previous measurements. Lack of order in a ferromagnetic state for this system indicates that it needs to be understood for a clear understanding of its ground state spin dynamics.

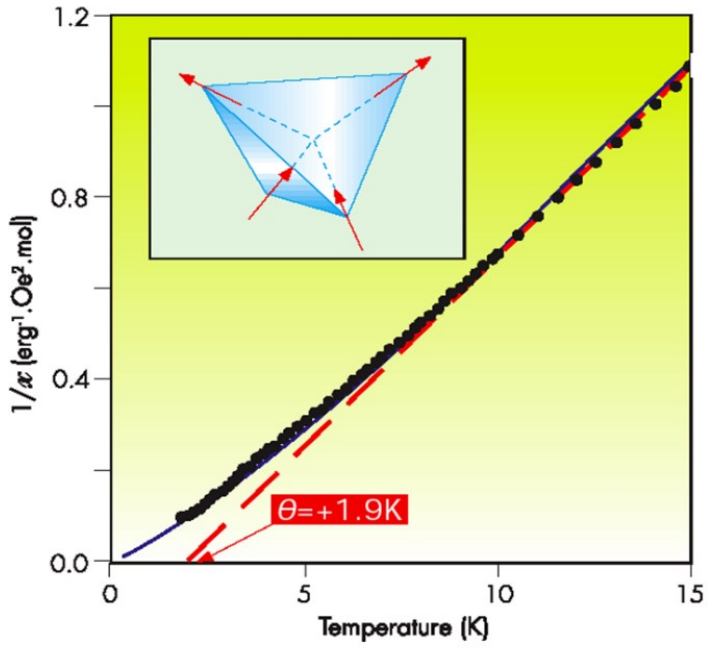

Figure 1.21 χ-1 vs. T plot for $Ho_2Ti_2O_7$ providing the value of $\theta_{CW} = +1.9 \pm 0.1$ K in accordance with Curie-Weiss law. [57]

Till now, the associated studies yield a reasonably successful quantitative theory of spin-ice behavior in Ising pyrochlores; however, the reason, why long-range dipolar interactions do not appear to lift the macroscopic degeneracy associated with the ice rules and select an ordered state is still an open-ended problem.

Crystal field interaction and Single ion Anisotropy

The electrostatic potential acting as a sum of the ligand contributions is termed the crystal field potential and written as:

$$\hat{V}_{cf} = \sum_{i=1}^{n} \sum_{L=1}^{N} \frac{1}{4\pi\epsilon_0} \frac{-eq_L}{|\vec{r_i} - \vec{R}_L|} = \sum_{i=1}^{n} \hat{v}_i \qquad (1.30)$$

The individual terms of the one-electron operator $\hat{v}_i$ is written as

$$\hat{v}_i = \frac{e^2}{4\pi\epsilon_0} \sum_{L=1}^{N} \frac{q_L^0}{|\vec{r_i} - \vec{R}_L|} \qquad (1.31)$$

where we assume that ligands bear the negative charges $q_L = -eq_L^0$. N is the number of ligands, n is the number of central metal ion, r is the metal ion coordinate, R is the ligand position.

According to crystal field theory, the neighboring orbitals are modelled as the negative point charges. The crystal field mainly arises from the electrostatic repulsion from the negatively charged electrons in the oxygen orbitals. The advanced systematic work on this approximation is ligand field theory, which essentially expands the molecular orbitals theory revealing the crucial character of d-orbitals on the central cation, which overlap with the nearby orbital of adjacent anions (ligands). The electric field exerted by this potential $\hat{V}_{cf}$ resulting from

neighboring ligands atoms of the crystal is known as crystal field. The crystal field interaction is set by the symmetry of the central metal ion, which sets up the energy level of an atom. The size and nature of the crystal field depend upon the crystallographic arrangement of the ligands (generally O^{2-} ion) around the metal ion.

As discussed in section 1.4 the conventional pyrochlore type of structure, say $Ho_2Ti_2O_7$ ($Ho_2Ti_2O_6O'$), there are six oxygen atoms (designated as O) around the central rare-earth ion forming an anti-prismatic structure [58]**.** There are two oxygen atoms (O') transverse of the anti-prismatic plane of six oxygen (O) atoms. The two oxygen atoms (O') are responsible for driving the local Ising anisotropy and sets a strong axial symmetry along a local <111> axis of the tetrahedron, as shown in **Figure 1.22**.

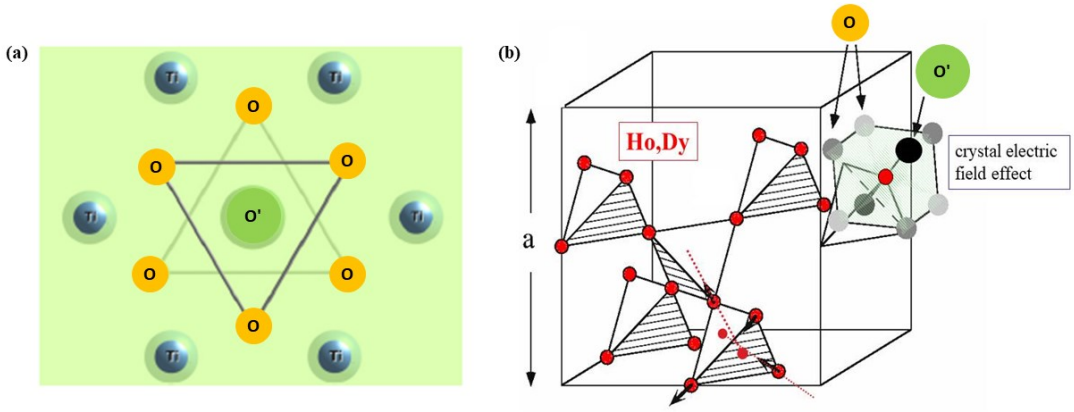

Figure 1.22 (a) Two oxygen atoms (O') are responsible for driving the local Ising anisotropy and sets a strong crystal-field effect along the <111> axis of the tetrahedron. (b) Strong axial symmetry of the magnetic site has along a local <111> direction. [58]

The states of a magnetic ion due to crystal field are markedly different because of their varying single ion properties. These crystal field levels decide the ground state magnetism. In rare-

earth ions, J (= L+S) is large and the spin-orbit coupling constant (λ) is proportional to Z^4. In pyrochlores this spin-orbit coupling constant (λ) is of the order of 1 meV. The energy scale set by the crystal field is of the order of 100 meV. The final energy, i.e., the exchange interactions, is relatively weak of the order of 0.1-1 meV due to the *f* electron being more spatially localized. Electrostatic and covalent bonding effects originating from the local crystalline environment lift the (2J+1) degeneracy of the ground state, which in turn determines the single-ion anisotropy of the ion. The spin-orbit interaction is given as

$$<\lambda L.S> = \lambda/2[J(J+1) - L(L+1)-S(S+1)] \quad (1.32)$$

which splits the (2S+1) (2L+1) levels into well-defined J manifolds, each with a degeneracy of 2J+1. In rare-earth, since λ is large, a well-isolated ground state J varies from |L-S| to |L+S|.

In case of Ho^{3+}, using the Hund's rule

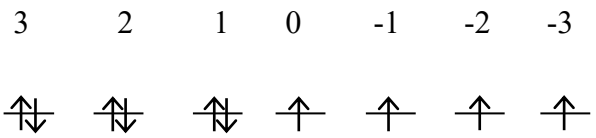

L = 6, S = 2, J= 8 & $\mu_{calc} = 10\ \mu_B/Ho^{3+}$.

$$\text{where } \mu_{calc} = g_J\sqrt{J(J+1)}\mu_B \quad (1.33)$$

and g_J is the Lande g-factor given by:

$$g_J = 3/2 + S(S+1) - L(L+1)/2J(J+1) \quad (1.34)$$

For the pyrochlore oxides, this crystal field originates from the oxygen anions. In cases of an odd electron count, the total spin is a half-integer, and Kramer's theorem applies, which is that every energy level must be at least doubly degenerate. In the case of integer spin systems,

Kramer's theorem does not apply, and the 2J + 1 levels can be maximally split in accordance with the site symmetry. The crystal field spectrum of Ho^{3+} ion is comprised of six doublets and five singlets, resulting in 2J + 1 = 17 energy levels. The CF Hamiltonian for this D_{3d} point group symmetry of Ho^{3+} in pyrochlore $Ho_2Ti_2O_7$ is further elucidated in terms of O_q^k which is the Stevens's operator and B_q^k. B_q^k is the C.F. parameter, which considers the charge effect of ions that surrounds the Ho^{3+}. In terms of both these parameters, the CF Hamiltonian is expressed as $\hat{H}_{CF} = \tilde{B}_\circ^2\hat{O}_\circ^2 + \tilde{B}_\circ^4\hat{O}_\circ^4 + \tilde{B}_3^4\hat{O}_3^4 + \tilde{B}_\circ^6\hat{O}_\circ^6 + \tilde{B}_3^6\hat{O}_3^6 + \tilde{B}_6^6\hat{O}_6^6$ where O_q^k is a function of J = (J_x,J_y,J_z), i.e., the total angular momentum of Ho^{3+} spins. The coupling of the total angular momentum to the transverse magnetic field can be written in terms of ladder operators as

$$\hat{J}.B_\perp = ½\,|B_\perp|\,(e^{-i\Phi}\hat{J}_+ + e^{i\Phi}\hat{J}_-) \qquad (1.35)$$

In the local coordinate system, Φ is the angle of the field with respect to $\mathbf{x}_0$ in the plane transverse to the easy axis $\mathbf{z}_0$, as shown in **Figure 1.23 (a)** [58]**.** The dependence of the splitting of the ground-state doublet $\Delta E_{01} = E_1 - E_0$ versus the magnitude of the transverse field and Φ is shown in **Figure 1.23 (b & c).** CF Hamiltonian is diagonalized to obtain the single ion crystal field spectrum, which is expressed in terms of quantum number |J, M_j>, M_j is the projection of correlated 4f electrons of Ho^{3+} along |111> axis of the tetrahedron.

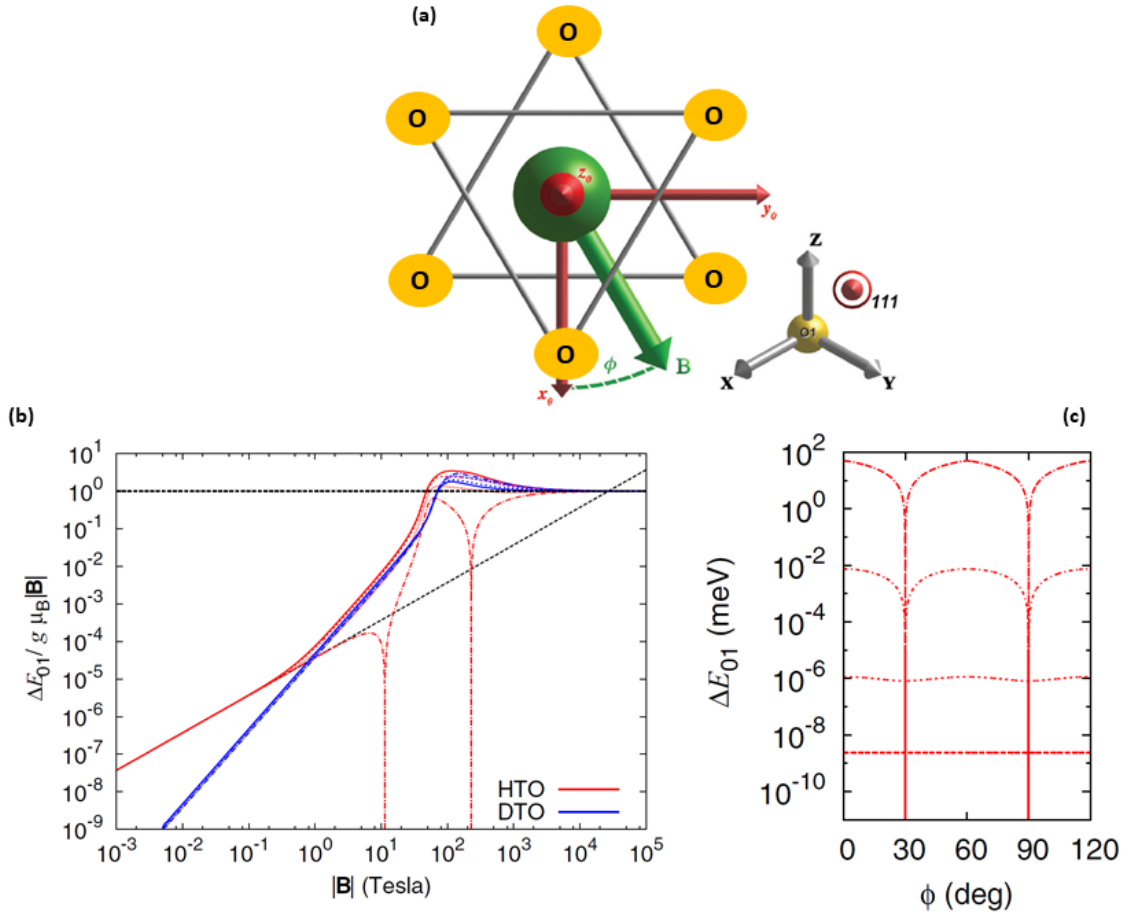

Figure 1.23 (a) The local coordinate frame x_0,y_0,z_0 (red arrows) used to describe the transverse magnetic field B (green arrow) and its direction angle Φ in Eq. (1.35). (b) Splitting of the ground-state doublet under the influence of a purely transverse magnetic field. The red curves correspond to the non-Kramers behavior of $Ho_2Ti_2O_7$. (c) Splitting of the ground-state doublet $\Delta E_{01} = E_1 - E_0$ versus the magnitude of the transverse field. [58]

The electronic parameters for Ho^{3+} are listed below:

[R]	$[R^{3+}]$	S	L	J	GS	g_J	μ	Δ (meV)	Δ (K)
$[Xe]4f^{11}\,6s^2$	$[Xe]4f^{10}$	2	6	8	|8, ±8>	5/4	~ 10 μ_B	~0.020	~ 240 K

The spectrum of $Ho_2Ti_2O_7$ featuring five singlets and six doublets is shown in **Figure 1.24** [58].

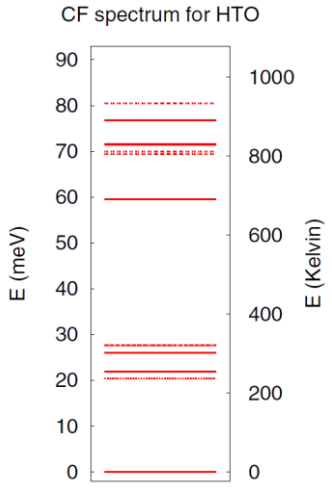

Figure 1.24 Crystal field spectrum of $Ho_2Ti_2O_7$ features six doublets (solid lines) and five singlets (dashed-dotted lines). In meV, bottom to top, the series of doublets is 0, 21.96, 25.99, 59.59, 71.51, and 76.80, while the series of singlets is 20.42, 27.71, 69.36, 69.94, and 80.52. [58]

1.9 Application of chemical pressure in magnetically frustrated systems (dipolar spin ice model)

As explained in section 1.8, $Ho_2Ti_2O_7$ lacks long-range ordering, yet the dipolar spin ice model (DSIM), as shown in **Figure 1.1,** presents the possibility for long-range ordering by varying the complex dipolar and exchange interaction. As could be seen from the inset of **Figure 1.1,** the specific heat vs. temperature exhibits two features, one at a T = 0.2 K and the other at T = 1 K. The transition for T = 1 K corresponds to a first-order phase transition to spin-ice state, whereas T = 0.2 K is related to a second-order phase transition to long-range ordered Néel state with the spin arrangement of "all in-all out" configuration. Phase diagram of Ising pyrochlore magnet reveals that spin ice configuration persists till "J_{nn}/D_{nn}~ -0.91" and

it lies in the stable regime. For "$J_{nn}/D_{nn} < -0.91$", the system undergoes a second-order phase transition to Q = 0 phase, where spins follow "all in-all out" configuration in tetrahedron as shown in **Figure 1.25** [59]**.**

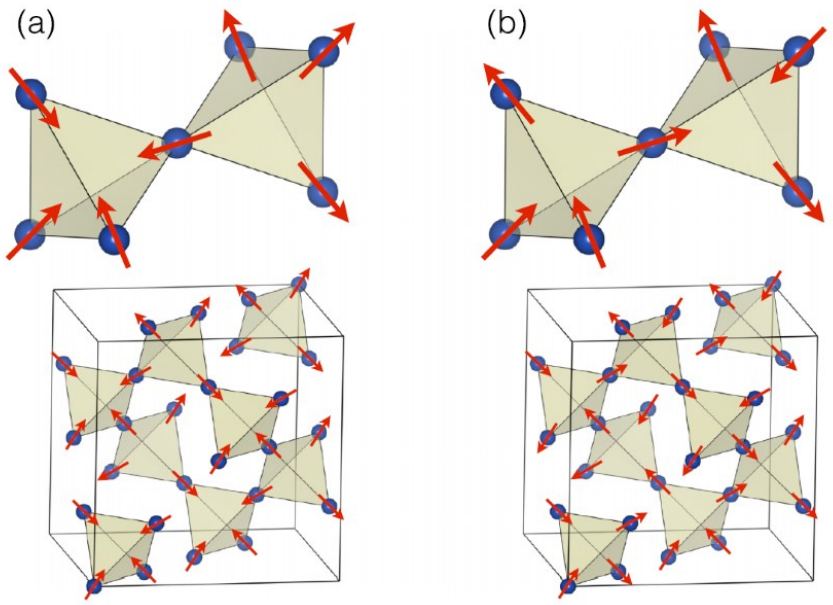

Figure 1.25 The two competing phases for spin-ices: (a) the Q = 0 "all in-all out" phase and (b) the spin-ice "two in-two out" phase. [59]

The dipolar spin-ice Hamiltonian can be expressed as:

$$H = -J_{nn} \sum_{<i.j>} S_i . S_j + D_{nn} r_{nn}^3 \sum_{i>j} \left[\frac{S_i . S_j}{|r_{ij}|^3} - \frac{3(S_i . r_{ij})(S_j . r_{ij})}{|r_{ij}|^5} \right] \quad (1.36)$$

Where J_{nn}, D_{nn}, and r_{nn} are respectively an antiferromagnetic exchange coupling, the dipole-dipole coupling constants, and the nearest neighbor distance between the rare-earth ions; *i* and *j* label the sites of pyrochlore lattice; $\overrightarrow{S_i} = \sigma_i \vec{z}_i$; $\sigma_i = \pm 1$ and $\vec{z}_i$ are four inequivalent unit vectors pointing from one tetrahedral sublattice to another); r_{ij} is the distance between two sites *i* and *j*. This equation presents the comprehensive quantitative description of spin-ice materials.

Here, J_{nn} is the free parameter, while D_{nn} is defined through dipolar interaction using the value of r_{nn} = 3.5 Å for $Ho_2Ti_2O_7$.

$$D_{nn} = \frac{\mu_0 \mu^2}{4\pi r_{nn}^3} \sim 1.4 \text{ K.} \quad (1.37)$$

The numerical estimate of J_{nn} for $Ho_2Ti_2O_7$ is obtained through a comparison between Monte Carlo simulations and experimental data for neutron scattering (ref). The dipolar interaction between spin *1* and spin *2* can be defined as:

$$D r_{nn}^3 \left[\frac{S_1.S_2}{|r_{12}|^3} - \frac{3(S_1.r_{12})(S_2.r_{12})}{|r_{12}|^5}\right] = \frac{5D}{3}\ \sigma_1\sigma_2 \quad (1.38)$$

Hence the nearest neighbor term of the dipolar interaction is equivalent to an exchange term, and the nearest neighbor spin-ice Hamiltonian as mentioned in equation (1.36) could be expressed as:

$$H = -3J_{eff} \sum_{<i,j>} S_i S_j = J_{eff} \sum_{<i,j>} \sigma_i \sigma_j \quad (1.39)$$

where $J_{eff} = D_{nn} + J_{nn} = \frac{5D}{3} + \frac{J}{3}$,

The role of chemical pressure on the nearest neighbor exchange, dipolar and effective antiferromagnetic coupling can be seen for $Ho_2Ti_2O_7$ and $Ho_2Sn_2O_7$ system as listed below,

Compound	D (K)	D_{nn} (K)	J (K)	J_{nn} (K)	J_{eff} (K)
$Ho_2Ti_2O_7$	1.41	2.35	-1.65	-0.52	~ 1.8
$Ho_2Sn_2O_7$	1.41	2.35	~1.0	~0.33	~2.7

It could be inferred that variation in both the exchange and dipolar interaction through the variation in chemical pressure would shift the system towards the AFM phase boundary and can induce long-range ordering in the spin-disordered system. To date, no Ho^{3+} pyrochlore system has been reported to transit beyond -0.91 (J_{nn}/D_{nn}) in the phase diagram proposed on

the basis of DSIM [60]. Due to very small energy scales of exchange Hamiltonian relative strength of various possible interactions varies with subtle changes in temperature. The detailed picture of ground-state spin relaxation is also a matter of investigation.

1.10 Previous results in relevance to the application of chemical pressure

T. Stöter *et al.* reported the tuning of the interaction in $Dy_2Ge_{2-x}Si_xO_7$ through silicon substitution. **Figure 1.26 (a)** presents the real (χ') and imaginary (χ") part of ac-susceptibility for three frequencies [21]. Frequency dependence is clear in χ" where peak sharpness increases with decrease in frequency from 770 Hz to 16 Hz. The transition temperature also shows considerable composition dependence for both x =0 and x = 0.125 in $Dy_2Ge_{2-x}Si_xO_7$. τ_o (spin relaxation time) also differs for both the compositions which is 250 ns for x = 0 and it reduces to 90 ns for x = 0.125 as shown in **Figure 1.26 (b),** This indicates that chemical pressure could tune the spin tunneling rate between two ground state Ising doublet spin states. The magnetic entropy for both $Dy_2Ge_2O_7$ (black symbols) and $Dy_2Ge_{1.875}Si_{0.125}O_7$ has been compared and have been calculated using the temperature dependence of the magnetic specific heat as shown in **Figure 1.27 (a).** The magnetic entropy is shown in **Figure 1.27 (b).** We obtain a different value of the ground-state entropy with 1.62 $Jmol^{-1}{}_{Dy}K^{-1}$ ($Dy_2Ge_2O_7$) and 1.31 $Jmol^{-1}{}_{Dy}K^{-1}$ ($Dy_2Ge_{1.875}Si_{0.125}O_7$). Noting the value of specific heat and T_{peak} from **Figure 1.27 (a),** J_{nn}/D_{nn} ratio was obtained that goes from -0.71 ($Dy_2Ge_2O_7$) to -0.74 ($Dy_2Ge_{1.875}Si_{0.125}O_7$).

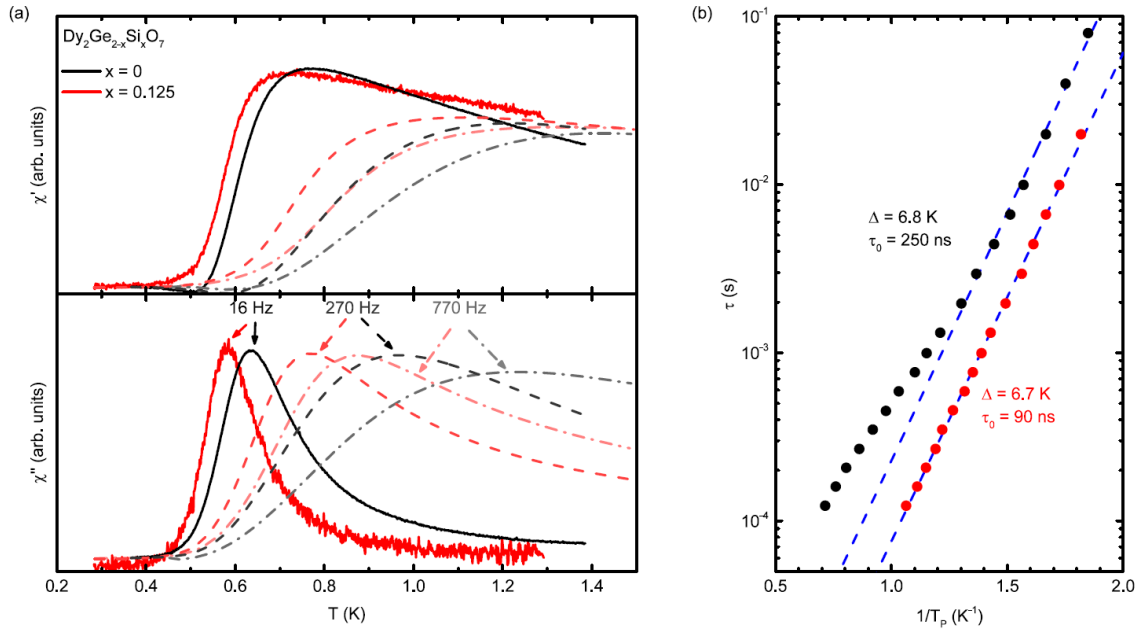

Figure 1.26 (a) Real and imaginary parts of the ac susceptibility of $Dy_2Ge_2O_7$ (black lines) and $Dy_2Ge_{1.875}Si_{0.125}O_7$ (red lines) at frequencies of 16 Hz (solid lines), 270 Hz (dashed lines), and 770 Hz (dash-dotted lines). (b) Spin-relaxation time τ as a function of the inverse peak temperature T_P used for Arrhenius fit. [21]

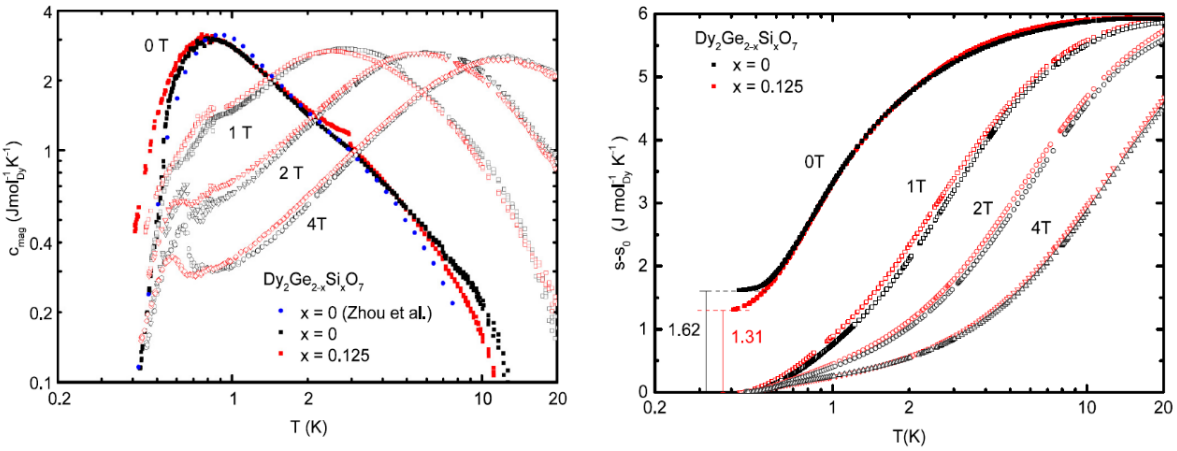

Figure 1.27 (a) Temperature dependence of the magnetic specific heat c_{mag} per mol of Dy of $Dy_2Ge_2O_7$ and $Dy_2Ge_{1.875}Si_{0.125}O_7$ samples. (b) Temperature dependence of the molar entropy of $Dy_2Ge_2O_7$ and $Dy_2Ge_{1.875}Si_{0.125}O_7$ at zero fields and 1, 2, and 4 T. [21]

Figure 1.28 presents the magnetic response in the ac-susceptibility of $Dy_{2-x}Yb_xTi_2O_7$ with the application of chemical pressure as reported by Hui Liu *et al.* [61].

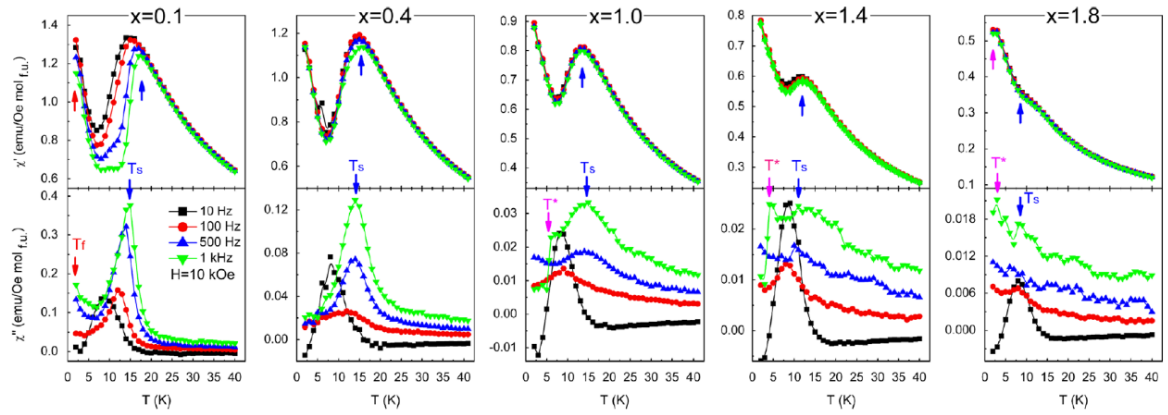

Figure 1.28 The real (χ′) and imaginary part (χ″) of ac-susceptibility of $Dy_{2-x}Yb_xTi_2O_7$ measured at H = 10kOe. [61]

It suggests the weakening in the FM coupling with an increase in frequency, as could be seen from the shift of T_f towards lower temperature. There happens a remarkable effect of chemical pressure on the single ion freezing temperature (T_s). With the increase in chemical pressure ($x > 0.1$; $Dy_{2-x}Yb_xTi_2O_7$), T_s becomes independent of frequency, indicating that the spin relaxation mechanism is attributed to the quantum mechanical process. The discussed measurements serve as a good result for tuning the interaction parameter with the application of the chemical pressure effect.

1.11 Holmium pyrogermanate

Pyrogermanates ($A_2Ge_2O_7$; A = rare earth element) possess a completely different structure compared to conventional cubic pyrochlore and belongs to a tetragonal class of crystal system under ambient preparation conditions with $P4_12_12$ space group [28], [62]. $A_2Ge_2O_7$ manifest

themselves in tetragonal (A = Eu, Tb-Lu), triclinic (R = La, Pr or Nd, Gd), and even monoclinic structures ($Sc_2Ge_2O_7$) [20]. Smolin (1970), Chiragov *et al*. (1983), and Geller and Gaines (1987) presented the structural analysis of $Er_2Ge_2O_7$, $Eu_2Ge_2O_7$, and $Tb_2Ge_2O_7$, respectively [64], [65]. Pyrogermanates lies outside the structural stability regime for pyrochlore, the range for which is 1.36-1.71. For $Ho_2Ge_2O_7$, the value for the same is $R_{Ho^{3+}}/R_{Ge^{4+}}$ = 1.8 [62]. Pyrogermanate having an entirely different crystallographic structure than the titanates also belong to the spin ice family in which the ice like configuration is expected to originate from the spiral structure of magnetic ions, as shown in **Figure 1.29 (a).** It shows the crystal structure of $Ho_2Ge_2O_7$ with the sublattice of rare earth Ho^{3+} showing the right-handed helices centred on fourfold screw axes parallel to the c-axis; the edge-sharing triangles connecting the Ho atoms are shaded. The Ho-O and Ho-Ge coordination polyhedra are shown in **Figure 1.29 (b)** and **Figure 1.29 (c),** respectively. Magnetic spin configuration showing eight Ho ions in four equivalent ab planes, **Figure 1.29 (d)**. The magnetic configuration and its response to the temperature and structure make these pyrochlore systems a suitable candidate to study the magnetic frustration since spin relaxation identically corresponds to pyrochlore systems, as shown in **Figure 1.30.**

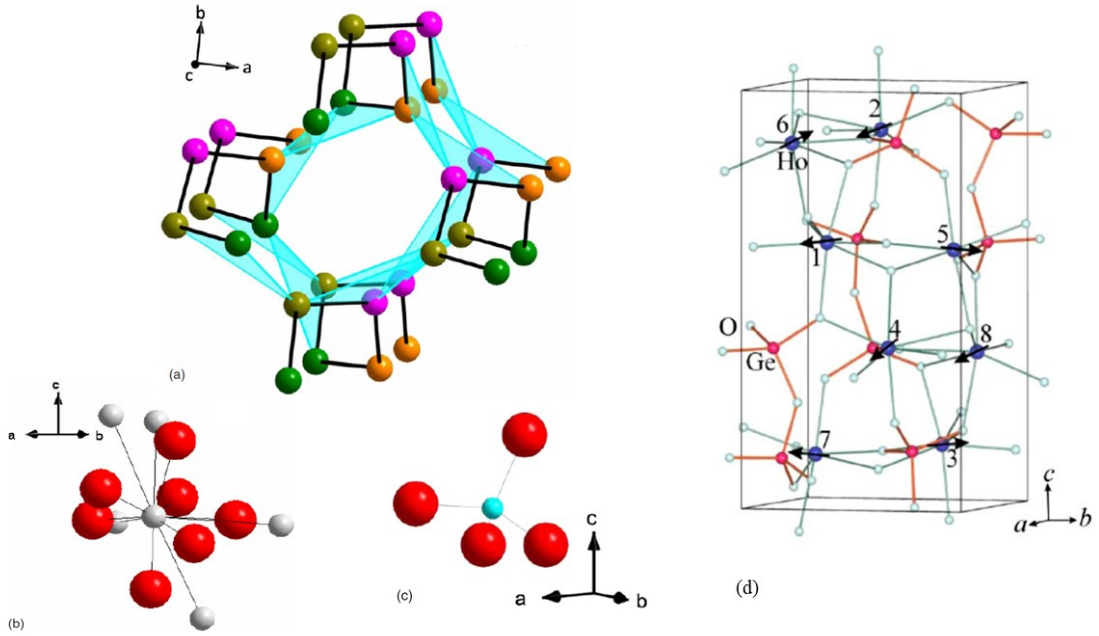

Figure 1.29 Crystal structure of $Ho_2Ge_2O_7$ (a) the rare earth Ho sublattice showing the right-handed helices centred on fourfold screw axes parallel to the c-axis; the edge-sharing triangles connecting the Ho atoms are shaded. The different colored atoms illustrate the four Ho atoms around the fourfold screw axis. (b) the Ho-O and (c) Ho-Ge coordination polyhedra, with Ho—red (dark gray) and O/Ge—white/light blue (light gray): there are five O in a highly distorted pentagon in the ab plane, and two more O, one above and one below. (d) Magnetic spin configuration showing eight Ho ions in four equivalent ab planes. [28]

The temperature-dependent anisotropic magnetization measurements of a single crystal of tetragonal $Ho_2Ge_2O_7$ for field $H \| ab$ (circles) and $H \| c$ (triangles) are shown in **Figure 1.31 (a)**. The left inset indicates the absence of magnetic ordering down to the lowest measured temperature of T=1.8 K. The larger values of magnetization for the field applied parallel to the *ab* plane circles than for $H \| c$ indicates that the spins lie close to the *ab* plane. The anisotropic inverse susceptibility responses are linear at high temperatures for both $H \| ab$ and $H \| c$, with the $H \| c$ data displaying a broad peak around 60–80 K (right inset **Figure 1.31 (a)**.

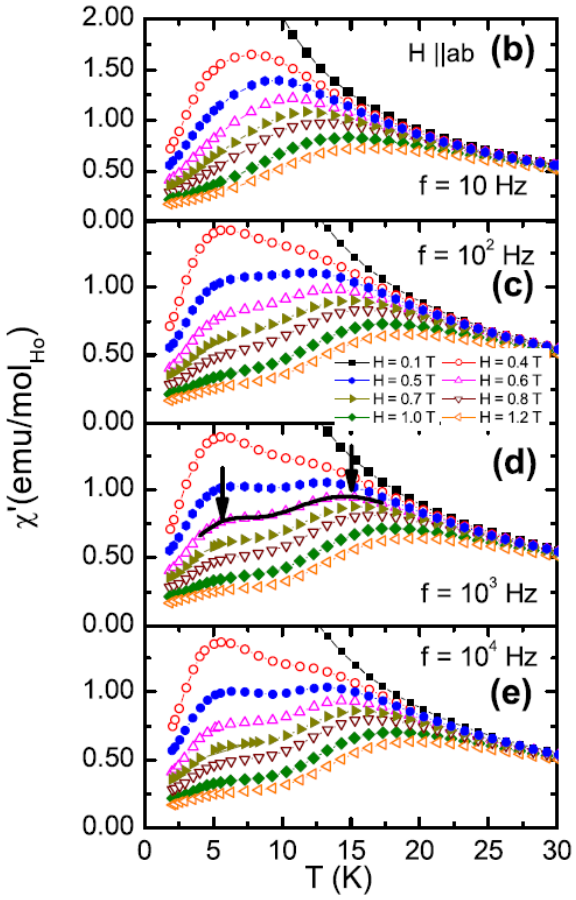

Figure 1.30 ac-susceptibility data for single crystal of $Ho_2Ge_2O_7$ when magnetic field is applied parallel to ab axis; (b)-(e) ν = 10, 102, 103, and 104 Hz data for H= 0.1, 0.4, 0.5, 0.6, 0.7, 0.8, 1.0, and 1.2 T.[28]

The possibly associated reason for this broad peak is the crystal electric field anisotropy. The "hard axis" $H \| c$ susceptibility increases at lower temperature as if approaching a low-temperature magnetic ordering. The specific heat data of $Ho_2Ge_2O_7$ shown in **Figure 1.31 (b)** confirms the presence of a transition temperature below 1.6 K, and this explains the local minimum observed in the $H \| c$ susceptibility in the right inset of **Figure 1.31 (a).** The T =2 K magnetization vs. field response, as shown in **Figure 1.31 (c),** also supports the planar magnetic anisotropy picture.

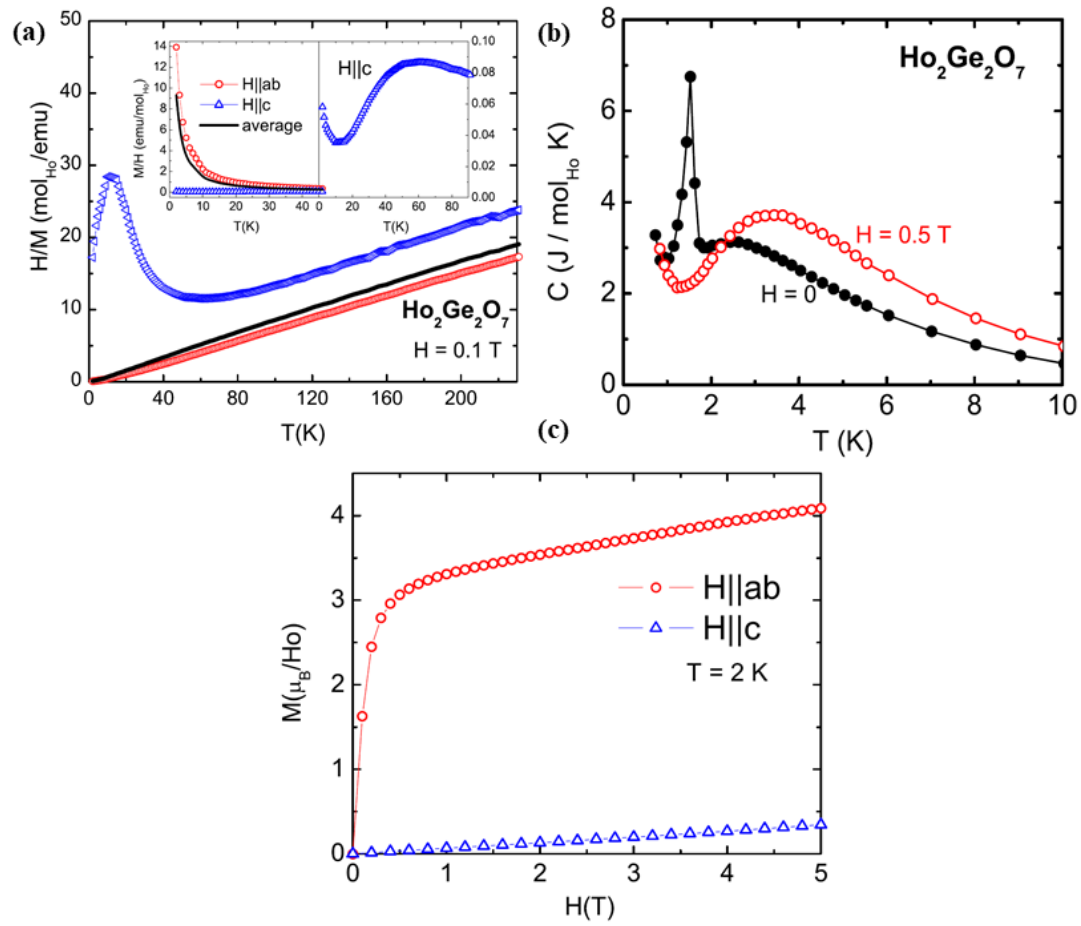

Figure 1.31 Inverse magnetic susceptibility of $Ho_2Ge_2O_7$ (single crystal) for H = 0.1 T and H||ab (circles) and H||c (triangles) together with the calculated average inverse susceptibility (line). Inset: low temperature anisotropic susceptibilities. (b) Specific heat for $Ho_2Ge_2O_7$ measured at zero and applied field (0.5 T). (c) T = 2 K M(H) isotherms for H||ab (circles) and H||c (triangles). [28]

The $H \| c$ axis magnetization is small and linear up to our maximum field of H = 5 T, as expected for the hard magnetization direction and field values smaller than the CF energy. For the field applied within the *ab* plane, a sharp increase of the magnetization below H = 1 T is followed by a plateau with a finite positive slope, attributable to the magnetization slowly rising toward saturation. Unlike $Ho_2Ti_2O_7$, $Ho_2Ge_2O_7$ belongs to a class of magnetically

frustrated spin disordered systems, which shows a higher transition temperature related to magnetic ordering at 1.6 K. Also, a thorough analysis of this structure would be interesting due to its distinctive pentagonal D_{5h} crystal field site symmetry of Ho^{3+} ion in $Ho_2Ge_2O_7$, sorely seen in the $4f^n$ system [24].

1.12 Applications and motivations

Transition metal oxides possessing an explicit pyrochlore type structure had been extensively studied as it presents a varying range of physical phenomenon amongst all frustrated magnetic materials. Rare earth pyrogermanates has acquired extensive recognition, particularly due to their optical properties, circular dichroism (CD) spectra, magnetic susceptibilities, specific heat, etc. Mainly we have tried to focus on the magnetic studies of these pyrochlore oxides since such systems manifest rich magnetic properties. Along with the magnetic properties, electronic and optical studies had been performed to understand its application from these viewpoints too. Since a lot of theoretical magnetic models had already been proposed described through well-defined interaction Hamiltonian, the suggested study imparting chemical pressure provides for a better understanding of experimental findings in the context of magnetism and the underlying spin dynamics. All device and diagnostic applications are also dependent on the type of materials ranging from metal to insulator to semiconductor; henceforth, understanding ground state magnetism in these novel pyrochlore oxide materials from a fundamental perspective is necessary [18].

1.13 Thesis aim

In previous studies, the effects of the application of chemical pressure effect had been studied by varying the B site atom in $A_2B_2O_7$. Zhou *et al.* have studied both $Ho_2B_2O_7$ and $Dy_2B_2O_7$ series by replacing the B site atom in order of increasing ionic radii (B=Sn, Ge, Ti) and the ground state magnetic interaction is studied. In the $Ho_2Ge_xTi_{2-x}O_7$ system, we have fractionally substituted a smaller ionic radii atom (Ge) at the Ti site and vice versa to fine-tune the J_{nn}/D_{nn} ratio for examining any phase transition happening by inducing structural distortion in the $Ho_2Ti_2O_7$ /$Ho_2Ge_2O_7$ matrix.

- Chapter 1 accounts for the introduction and works of literature survey regarding the aspects studied in this thesis work. In chapter 2, we have studied the procedures and experimental techniques adopted to synthesize and characterize the materials.
- In chapter 3, we have discussed the synthesis of $Ho_2Ge_2O_7$ and studied its crystallographic structure in detail through HRXRD measurements. Further, the magnetic properties were discussed through magnetization vs. temperature, magnetization vs. the magnetic field, and frequency-dependent ac susceptibility measurements.
- In chapter 4, we have demonstrated the robust spin-ice freezing in $Ho_2GexTi_{2-x}O_7$ (x = 0,0.1,0.15 & 0.25) through the application of chemical pressure effect. The ac-susceptibility measurements suggested crystal field phonon coupling in $Ho_2GexTi_{2-x}O_7$ (x = 0,0.1,0.15 & 0.25). The parameters affecting the spin dynamics were investigated, namely the relative strength of J_{nn} (exchange interaction) and D_{nn} (dipolar interaction). Magnetic properties are further evaluated from magnetization versus

temperature, magnetization versus the field, and field-dependent ac susceptibility measurements.

- Chapter 5 deals with the calculation of the electronic structure of pyrochlore ($Ho_2Ti_2O_7$) and pyrogermanate ($Ho_2Ge_2O_7$) along with $Ho_2GexTi_{2-x}O_7$. The density of states and band structure were calculated along with the theoretical determination of the bandgap. The various states involved in hybridization for band formation were identified. Using the band structure, we recognized the high symmetry points involved in direct band transition. For indirect transitions, the phonon modes involved were also identified using the Brillouin zone for $Ho_2Ge_2O_7$ (space group; 92) and for $Ho_2Ti_2O_7$ (space group; 227).
- In chapter 6, the bandgap of $Ho_2GexTi_{2-x}O_7$ was experimentally calculated using UV-Visible absorption spectra. The complex pattern of UV-Visible absorption and photoluminescence emission spectra were used the identify the states for the same. Well agreement was established between the theoretical and experimental bandgap values. Precise wavelength-controlled luminescence spectra involving $^5I_8$ and $^5F_5$ electronic states have been presented. The result provides chemical pressure as an excellent tool to tailor the bandgap values in such magnetically frustrated systems.
- Chapter 7 summarizes the entire thesis work and provides a few suggestions for future work.